TASK-BASED IMAGE QUALITY ASSESSMENT IN RADIATION THERAPY

A Dissertation presented to
the Faculty of the Graduate School
at the University of Missouri-Columbia

In Partial Fulfillment
of the Requirements for the Degree
Doctor of Philosophy

By STEVEN DOLLY

Dr. Sudarshan Loyalka and Dr. Hua Li, Dissertation Supervisors

MAY 2016

The undersigned, appointed by the dean of the Graduate School, have examined the dissertation entitled

TASK-BASED IMAGE QUALITY ASSESSMENT
IN RADIATION THERAPY

presented by Steven Dolly,

a candidate for the degree of doctor of philosophy,

and hereby certify that, in their opinion, it is worthy of acceptance.

_____

Professor Sudarshan Loyalka

_____

Professor Hua Li

_____

Professor Tushar Ghosh

_____

Professor Lixin Ma

_____

Professor Mark Prelas

_____

Professor Robert Tompson Jr.

To my wife, for being there when I need her most.

To my parents, for seeing this through till the end

ACKNOWLEDGEMENTS

First, I would like to thank Dr. Hua Li, for providing the opportunity to research within the field of medical physics at Washington University in Saint Louis over these last three years, in addition to her supervision throughout my dissertation work and other projects.

I would also like to thank Dr. Mark Anastasio, for his very helpful contributions and discussion regarding medical imaging and task-based image quality assessment theory. Likewise, I would like to thank Dr. Hsin-Chen Chen for his helpful insight and discussion pertaining to geometric modeling and statistical shape analysis.

Finally, I would like to thank the faculty at the Nuclear Science and Engineering Institute at the University of Missouri. Specifically, I would like to thank Drs. Sudarshan Loyalka and Tushar Ghosh, for advising me in my coursework and research. I would also like to thank Drs. Lixin Ma, Mark Prelas, and Robert Tompson, for participating in my dissertation committee in addition to teaching relevant courses as a part of my doctoral education.

TABLE OF CONTENTS

ACKNOWLEDGEMENTS ii

LIST OF ILLUSTRATIONS vi

LIST OF TABLES viii

LIST OF ABBREVIATIONS ix

ABSTRACT xi

CHAPTER 1: INTRODUCTION 1
- A. Radiation Therapy 2
- B. Imaging in Radiation Therapy 3
- C. Current Image Quality Assessment in Radiation Therapy 5
- D. Task-Based Image Quality Assessment 7
- E. Dissertation Purpose & Outline 8

CHAPTER 2: AN OVERVIEW OF IMAGE QUALITY ASSESSMENT 11
- A. Physically-Based Metrics 11
  - A.1. Mean & Standard Deviation 12
  - A.2. Contrast-to-Noise Ratio 12
  - A.3. Fourier-Based Metrics 13
    - A.3.1. Noise Power Spectrum 14
    - A.3.2. Modulation Transfer Function 16
- B. Human Visual System (HVS) Based Metrics 17
  - B.1. Structural Similarity Index 18
- C. Task-Based Image Quality Assessment 20
  - C.1. Image System Modeling 21
  - C.2. Task Definition 22
  - C.3. Ideal Model Observer Derivation 22
  - C.4. Other Common Model Observers 25
- D. Task-based IQA for Radiation Therapy: The TOC Curve 26
  - D.1. TOC Curve Concept 26
  - D.2. TOC Curve Estimation 28
  - D.3. Simplification for External Beam Radiation Therapy 30

CHAPTER 3: A MODEL OBSERVER FOR TASK-BASED IQA IN RADIATION THERAPY 33
A. Model Observer General Strategy 33
B. Model Observer Implementation Schematics 35
C. Treatment Site & Modality Selection 37
D. Programming Ideology 37

CHAPTER 4: SIMULATING REALISTIC IMAGES OF KNOWN OBJECTS 39
A. Object Modeling Using GAD Models 40
A.1. Inter-Structural Centroid Modeling Theory 42
A.2. Intra-Structural Shape Modeling Theory 43
A.3. Training Data Set Acquisition 44
A.4. GAD Model Training and Organ Generation 45
A.5. Object Model Creation 47
B. CT Projection Generation Using Exponential Attenuation 48
C. CT Image Reconstruction Using Filtered Backprojection 51
C.1. Projection Z-Filtering 51
C.2. Filtered Backprojection 52
C.3. Implementation Details 54
D. Results & Discussion 55

CHAPTER 5: SIMULATION FRAMEWORK IMPLEMENTATION 60
A. Semi-Automatic Image Segmentation Using ITK-SNAP 60
A.1. Pre-Segmentation Image Generation 61
A.2. Geodesic Active Contour Algorithm 63
B. Treatment Planning 64
B.1. Treatment Plan Initialization 64
B.2. Dose Calculation 66
B.3. Dose Optimization 67
C. Radiobiological Modeling 70
D. Results & Discussion 72

CHAPTER 6: MODEL OBSERVER APPLICATION & ANALYSIS 76
A. Application 1: Optimization of imaging dose 76
B. Application 2: Optimization of CT reconstruction algorithms 77
C. Analysis 1: Comparison to other IQA metrics 78
D. Analysis 2: Sources of randomness 80
E. Analysis 3: Sources of bias 81

F. Results & Discussion 82

CHAPTER 7: CONCLUSIONS AND FUTURE WORK 87

A. Summary of Contributions 87

B. Future Directions 90

REFERENCES 94

VITA 99

LIST OF ILLUSTRATIONS

Figure Number & Description	Page Number
Figure 1. Comparison of noise texture with NPS	14
Figure 2. A measured ESF with calculated MTF	16
Figure 3. SSIM comparison for multiple images	19
Figure 4. Sample plots of TCP and NTCP	27
Figure 5. The therapeutic operating characteristic curve	28
Figure 6. Radiation therapy model observer general strategy	34
Figure 7. Radiation therapy model observer specific design	36
Figure 8. Object generation methodology with GAD models	42
Figure 9. User interface for extraction of patient data	45
Figure 10. Signed distance function illustration.	46
Figure 11. Organ modeled as point cloud and triangular mesh	47
Figure 12. Relational organ hierarchy	48
Figure 13. The adjustable reconstruction filter	53
Figure 14. Inter-structural GAD centroid model training results	55
Figure 15. Intra-structural GAD shape model training results	56
Figure 16. Two samples of generated patient objects	57
Figure 17. Simulated CT images for varying parameters	58
Figure 18. ITK-SNAP pre-segmentation “speed image”	62
Figure 19. Dose optimization results	72
Figure 20. TCP, NTCP, and TOC curves	74
Figure 21. ROI placement for CNR and NPS calculation	79

Figure 22. Sample SSIM map for the acquired CT images 80

Figure 23. AUTOC as a function of CT imaging dose 83

Figure 24. AUTOC for different image reconstructions 84

Figure 25. Analysis of the radiobiological model bias 85

LIST OF TABLES

Table Number & Description	Page Number
Table 1. NIST materials utilized for the patient object models	49
Table 2. Region growing segmentation parameters	63
Table 3. The dose constraints for the treatment plan	65
Table 4. Radiobiological model parameter values	71

LIST OF ABBREVIATIONS

AUTOC	Area under the therapeutic operating characteristic
BKE	Background known exactly
CNR	Contrast-to-noise ratio
CT	Computed tomography
CTDI	CT dose index
DPM	Dose planning machine
DSC	Dice’s similarity coefficient
ESF	Edge spread function
EUD	Equivalent uniform dose
FBP	Filtered backprojection
FOM	Figure of merit
GAD	Geometric attribute distribution
HVS	Human visual system
IMRT	Intensity modulated radiation therapy
IQA	Image quality assessment
LSF	Line spread function
MRI	Magnetic resonance imaging
MTF	Modulation transfer function
NEQ	Noise equivalent quanta
NPS	Noise power spectrum
NTCP	Normal tissue complication probability
PCA	Principal component analysis
PDF	Probability density function

PET	Positron emission tomography
ROC	Receiver operating characteristic
ROI	Region of interest
SDR	Sigmoidal dose response
SKE	Signal known exactly
SNR	Signal-to-noise ratio
SSIM	Structural similarity index
SVD	Singular value decomposition
TCP	Tumor control probability
TOC	Therapeutic operating characteristic

TASK-BASED IMAGE QUALITY ASSESSMENT
IN RADIATION THERAPY

Steven Dolly

Dr. Sudarshan Loyalka and Dr. Hua Li, Dissertation Supervisors

ABSTRACT

Medical imaging is an integral part of radiation therapy, therefore image quality assessment (IQA) is important for improving patient treatments. Current IQA methods for radiation therapy do not directly consider the task of treating the patient. Many studies have been dedicated to task-based IQA, however almost exclusively for diagnostic imaging. The purpose of this dissertation is therefore to provide and demonstrate a robust, fully computer-simulated model observer. This observer utilizes images of known objects to simulate end-to-end radiation therapy treatments, and subsequently evaluates treatments in terms of patient outcome. Thus image quality is linked directly to patient treatment efficacy. As a necessary component, a methodology was also developed to generate statistical ensembles of objects, with subsequent CT images. Using this newly proposed model observer, CT images were assessed and optimized for the task of radiation therapy, and the results were demonstrated as an improvement to other IQA methods which do not consider the specific task of radiation therapy. The model observer was also insensitive to the sources of randomness and bias analyzed in this study. This model observer therefore enables objective, task-based IQA with radiation therapy treatment efficacy as the goal.

CHAPTER 1: INTRODUCTION

Medical imaging has become an integral part of radiation therapy treatments, as the resulting images are used to plan and deliver the radiation dose to the patient. Since these images directly affect patient treatment efficacy, image quality assessment is necessary for the comparison and optimization of imaging systems, with the goal of improving patient treatment outcomes. A variety of methods and metrics are used to assess image quality within radiation therapy, but none of them directly consider the task of treating the patient, as they are based solely on physical image properties. Meanwhile, a myriad of studies have been dedicated to task-based medical image quality assessment. In this task-based paradigm, mathematical and/or computerized model observers are often applied to assess images based on the ability to perform relevant clinical tasks. However, this task-based methodology has been applied almost exclusively for diagnostic imaging tasks, i.e. disease diagnosis. To fill the void of task-based image quality assessment in radiation therapy, the purpose of this dissertation is to provide and demonstrate a robust, fully computer-simulated model observer. This model observer will enable objective assessment and optimization of image quality with the goal of maintaining and even improving patient treatment outcomes. This chapter introduces general, relevant concepts and then provides an outline for the dissertation.

A. Radiation Therapy

Radiation therapy is a medical treatment that uses high-energy, ionizing radiation such as x-rays, gamma rays, and charged particles to treat disease. It is most often used to kill cancerous cells and shrink benign tumors, but can also be used to treat other diseases and conditions such as trigeminal neuralgia.[1–3] Radiation therapy can be delivered either externally by a machine outside of the patient (a process referred to as *external beam radiation therapy*) or internally by placing radioactive elements inside the patient near the disease (also known as *brachytherapy*). Ionizing radiation kills cells by damaging their DNA, and thereby rendering them incapable of reproducing. Unfortunately, during this process some normal tissue cells are also damaged; thus the ultimate aim of radiation therapy is to design and deliver a treatment which will maximize disease control while minimizing this damage to normal tissues.

The workflow for a typical radiation therapy treatment proceeds after the patient is diagnosed with a particular disease and a radiation therapy treatment is prescribed. The treatment process begins by acquiring relevant anatomical and physiological information about the specific patient. This information is then used to plan the delivery of an optimal radiation dose. During treatment planning the expected radiation dose delivered to the patient is estimated, given prior knowledge of the radiation source(s). Then this planned radiation dose is delivered in a consistent manner over the course of the treatment duration,

ranging from one day to a few months, with each individual treatment referred to as a *fraction*. To ensure treatment consistency, the patient is appropriately positioned relative to the treatment machine prior to the delivery of each fraction of radiation. While historically radiation therapy treatments were performed without medical imaging, today medical imaging has become an integral part of radiation therapy.

B. Imaging in Radiation Therapy

Prior to the incorporation of medical imaging, radiation therapy was performed using only the knowledge of the external boundary of the patient, without specific information regarding internal anatomy.[3] This external boundary, or contour, could be obtained using a metal wire or other mechanical device. Then the external contour was transferred to a sheet of paper, and two-dimensional treatment planning was performed, with the dose calculation done by hand. For dose calculation it was assumed that patient was comprised entirely of water.

However, the invention of x-ray computed tomography (CT) imaging in 1971 significantly improved the treatment planning process. In CT imaging, x-ray transmission measurements are acquired as a patient is scanned by a narrow beam of x-rays. Tomographic reconstruction is performed from these measurements to produce images of the patient. These CT images are now utilized to determine the size and location of both the tumor and surrounding

normal tissues. These structures can be delineated either manually or automatically using specialized computer software, a process most commonly referred to as *contouring* or *image segmentation*. Moreover, the pixel values from CT images, quantified using Hounsfield units, can be utilized to calculate the delivered dose to the patient for treatment planning purposes. This greatly improved the dose calculation accuracy by incorporating non-water tissue inhomogeneities (e.g. air, lung, bone). CT imaging thus revolutionized radiation therapy treatments by providing 3D information for treatment planning and atomic composition for radiation dose calculations, and is still a fundamental part of the treatment process.

Medical imaging is also utilized to aid other aspects of the radiation therapy treatment. For example, magnetic resonance imaging (MRI) is employed to assist in tumor and normal tissue segmentation, as these images have superior soft tissue contrast compared to CT images. As another example, imaging devices such as CT on-rails, cone-beam CT, ultrasound, and MRI are included in the same room as the therapy unit and are used to correctly position the patient daily prior to each treatment fraction. These images provide a means to adjust the patient's treatment based on inter-fraction motion (e.g. weight loss and organ size/shape) in addition to intra-fraction motion (e.g. breathing). Finally, biological and physiological tumor information can be obtained from functional imaging such as positron emission tomography (PET), and used to plan and optimize a patient's treatment. Medical images are therefore a crucial part of the

modern radiation therapy treatment, utilized for delineating the patient's organs, planning an optimized radiation dose, and positioning the patient correctly to ensure an accurate radiation dose delivery. Since these medical images are a determining factor in the efficacy of a patient's treatment, these images must be of adequate quality, introducing a need for image quality assessment.

C. Current Image Quality Assessment in Radiation Therapy

The discipline of image quality assessment (IQA) is primarily focused on the establishment of standards which answer one fundamental question: what constitutes a good image (or, more generally, a good imaging system)? Image quality can be assessed in a variety of ways, but it's assessment often includes three image properties: contrast (image intensity between two objects), spatial resolution (the ability to resolve small objects), and noise (statistical fluctuations in the image intensity).

IQA can be subjective, as when for example a human observer assigns a number from a rating scale (e.g. 1-5) to an image to state it's quality. As another example, a human observer could detect and report the distinguishably visible number of line pairs per millimeter on an image to assess system spatial resolution.[4] Such measurements have inherent variability, as different results could be obtained for the same image using different human observers. In addition, subjective approaches require significant human involvement,

increasing human workload. For these reasons subjective assessment is not ideal for IQA.

To remove result variability, images can instead be assessed objectively using physically-based image metrics. One common example is the standard deviation, which is often applied to a region of interest (ROI) in an image to quantify image noise. Other examples include Fourier-based metrics such as the modulation transfer function (MTF) for spatial resolution and the noise power spectrum (NPS) for image noise. Using these physically-based metrics, images can be compared, and those with higher spatial resolution and lower image noise are considered to have better image quality. These metrics, while improving upon the subjective assessment by providing objective quantitative consistency, can vary depending on the specific calculation parameters and ROI location.[5] Also, these measurements individually do not give any indication as to how helpful the images are for performing relevant clinical tasks, such as disease diagnosis, image segmentation, or disease treatment.

Another IQA method is the use of human visual system (HVS) models to determine the perceptual difference between multiple images. The most common of these is the structural similarity index,[6] which compares the intensity and structural similarity of images to a “gold standard” image. While this method improves upon the physically based metrics in that it is entirely objective and closely resembles a human observer, these methods cannot be used for images with opposing contrast values (e.g. T1 vs. T2 weighted MRI). Moreover, as with

the physically based metrics it is not possible to directly correlate HVS model metrics to system performance; external comparison to a desired task performance is still required.[7] Neither the physically-based metrics nor the HVS-based metrics consider the task of radiation therapy: to effectively treat the patient with radiation.

D. Task-Based Image Quality Assessment

Thus the paradigm of task-based IQA is introduced, which is based on the premise that image quality should be defined by the ability of an observer to perform a specific task using the available images. These observers may be human or model-based. Task-based IQA requires detailed knowledge of both the imaging system and the object that is being imaged, and is based on statistical decision theory. A large body of work exists describing and implementing task-based IQA for medical imaging.[8, 9] For example, given the task of deciding whether a disease (also referred to as the signal) is present or absent, many model observers have been derived which correlate imaging system characteristics such as the MTF and NPS to task performance. This evaluation is encapsulated within a singular scalar quantity referred to generally as the figure of merit (FOM), and in the case of this diagnostic imaging task is named the signal-to-noise ratio (SNR). The task-based FOM can be used to compare and assess images with the desired task in mind, and is therefore superior to the previously mentioned physically-based and HVS-based metrics.

However, unlike the diagnostic tasks which encompass a large majority of the medical imaging field, imaging in radiation therapy is performed with the overall goal of maximizing tumor control while minimizing the damage to normal tissues surrounding the tumor. Until recently the task-based assessment of image quality for radiation therapy tasks has not been studied. The initial effort (to the best of our knowledge) by Barrett *et al.*[10] provides some theory for objective IQA in radiation therapy. Radiation therapy treatment efficacy can be evaluated using the tumor control probability (TCP) and normal tissue complication probability (NTCP), evaluating the patient's quality of life post-treatment. In this work a therapeutic operating characteristic (TOC) curve is proposed as a FOM for radiation therapy, analogous to the receiver operating characteristic (ROC) curve,[8] with the TCP and NTCP spanning the axes and the delivered radiation dose as a hidden parameter. The area under the TOC (AUTOC) is presented as the FOM, which can be utilized for task-based IQA in radiation therapy.

E. Dissertation Purpose & Outline

While this work by Barrett *et al.* lays out some general theories for task-based IQA in radiation therapy and provides an adequate FOM, the implementation details are left undone. For example, the proposed methodology is prefaced on manual segmentation of clinical images by experts as the ground truth for patient data,[10, 11] excluding absolute ground truth assessment. Moreover,

to the best of our knowledge, task-based image quality assessment has not been applied to any aspect of radiation therapy. It is therefore the purpose of this dissertation to provide, for the first time, a robust, fully-computer-simulated model observer capable of task-based IQA for radiation therapy. Given CT images of a known object, the newly created model observer will perform task-based IQA by simulating an end-to-end radiation therapy treatment and subsequently evaluating the treatment by computing the AUTOC. Since the current methods for object modeling are inadequate for this model observer implementation, a new methodology for object modeling will also be developed. The fully simulated object modeling and CT imaging will enable absolute ground truth assessment. Since CT imaging is a crucial part of both image segmentation and dose calculation, the model observer will be demonstrated by optimizing CT images for radiation therapy. Additionally, the biases and limitations of this framework will be explored and understood. This model observer will enable both assessment and optimization of imaging devices for radiation therapy, in both the research and industry domains.

The remainder of the dissertation is structured as follows. Chapter 2 gives a detailed description of the current IQA methods, including the physically-based, HVS-based, and task-based metrics. The shortcomings of each methodology in relation to radiation therapy will be described, and a derivation of AUTOC calculation from the work of Barrett *et al.* will be given. Chapter 3 then provides a generalized description of the model observer, along with the implementation

ideology. Chapter 4 describes in detail the creation of a statistically relevant object modeling methodology, and the subsequent simulation of CT images from a known object model. Chapter 5 then describes the model observer implementation details, which involves a simulation of an end-to-end radiation therapy treatment, beginning with the generated CT images and resulting in the calculation of the AUTOC. Chapter 6 will apply the model observer by optimizing image quality for radiation therapy and comparing the outcome to the other aforementioned IQA metrics; this will demonstrate the potential and superiority of this model observer for radiation therapy. This chapter also assesses sources of randomness and bias within the model observer, to gain thorough understanding. Finally, Chapter 7 provides concludes the dissertation by summarizing the contributions and discussing the limitations and future potential of this model observer.

CHAPTER 2: AN OVERVIEW OF IMAGE QUALITY ASSESSMENT

In this chapter, the theory and current work of IQA will be summarized. This will provide context for the derivation of task-based IQA within radiation therapy, and will be necessary as the comparison is made between previously proposed metrics and the new model observer for radiation therapy. As subjective metrics will not be utilized within this study, the overview will begin with the physically-based metrics (Section A), followed by a description of HVS-based metrics (Section B). The chapter will conclude by providing a derivation for task-based image quality, both for disease diagnosis (Section C) and the AUTOC as proposed by Barrett *et al.* (Section D).

A. Physically-Based Metrics

Image quality can be assessed in a variety of ways, but it's assessment often includes three properties: contrast (image intensity between two objects), spatial resolution (the ability to resolve small objects), and noise (statistical fluctuations in the image intensity). Thus all the physically based metrics described here will encompass either one or more of these three properties. In the spatial domain these are the mean, standard deviation, and the contrast-to-noise ratio. In the Fourier domain, these are the noise power spectrum (NPS) and the modulation transfer function (MTF).

A.1. Mean & Standard Deviation

As images will contain noise and vary pixel-to-pixel even within a uniform object region, one important and fundamental image metric is the mean value of a ROI within the image. For a vector **g** containing *N* image pixel intensity values, the mean $\bar{g}$ can be calculated using Eqn. 1:

$$\bar{g} = \sum_{n=1}^{N} g_n \tag{1}$$

Here **g** can refer to the entire image or a ROI within the image and this vector can span any number of dimensions. Having determined the mean within a ROI, the statistical fluctuations with the ROI can be quantified by calculating the standard deviation σ:

$$\sigma = \sqrt{\frac{1}{N-1}\sum_{n=1}^{N}(g_n - \bar{g})^2} \tag{2}$$

These metrics provide a simple description of both the deterministic (mean) and stochastic (standard deviation) properties of an image, and can be combined to formulate other IQA metrics.

A.2. Contrast-to-Noise Ratio

For many signal detection tasks, it is often desired to quantify the balance between image noise and image contrast. One common metric to quantify this is the contrast-to-noise ratio (CNR). Given the mean intensity of the signal and

background, $\overline{g_s}$ and $\overline{g_b}$, respectively, and the corresponding standard deviation σ_s, the CNR can be calculated accordingly:[12]

$$CNR = \frac{|\bar{g}_s - \bar{g}_b|}{\sigma_s} \tag{3}$$

These metrics have served a variety of purposes in IQA. For example, in CT imaging the mean is used to assess CT number accuracy.[13] However, the limitation with this approach to IQA is that an inherent relationship between CT number, image noise, or CNR and clinical task performance does not exist; external comparison between these metrics and task performance is required.

A.3. Fourier-Based Metrics

While simple to calculate and utilize, the metrics listed above do not provide a comprehensive description of imaging system properties. For example, image ROIs with the same standard deviation can exhibit drastically different noise textures, which may significantly change task performance; Figure 1 illustrates such an example. To provide a more comprehensive description of these imaging system properties, Fourier-based analysis is employed, enabling an assessment of the contributions of individual spatial frequencies to image properties. The corresponding Fourier-based analysis of the image noise and spatial resolution are the noise power spectrum (NPS) and the modulation transfer function (MTF), respectively.

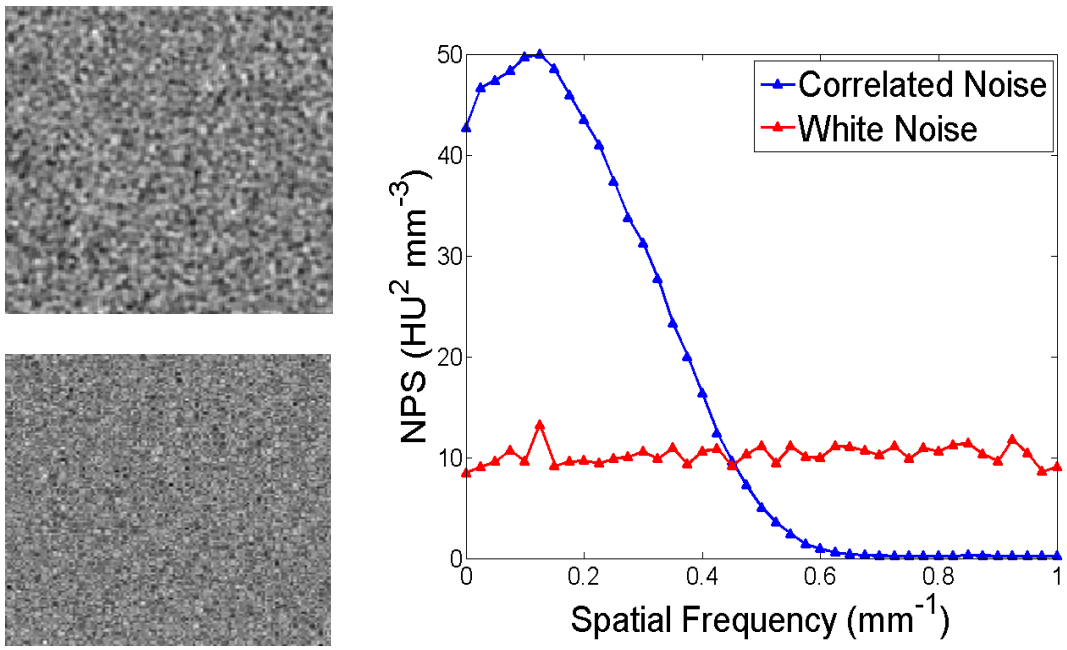

Figure 1. Two noisy image regions with same standard deviation, but different noise textures: one with correlated noise (top left) and one with white or Gaussian noise (bottom left). The plot (right) displays the difference in noise texture in terms of the noise power spectrum.

A.3.1. Noise Power Spectrum

The NPS of an acquired image vector $\mathbf{g}$ can be calculated by applying the discrete Fourier transform:[14]

$$NPS(f_i) = \mathbf{DFT}\{K_{i=j}\} = \langle|\mathbf{DFT}\{\mathbf{g_i} - \bar{\mathbf{g}}_\mathbf{i}\}|^2\rangle \quad (4)$$

Here *K* is the covariance matrix of the image data. Note that compared to Equation (1) both image vectors are in bold and there represent entire vectors instead of individual values. In other words, $\bar{\mathbf{g}}$ represents the expectation (i.e. mean) values of the image data while $\mathbf{g}$ represents a single image acquisition. When $\mathbf{g}$ represents the entire image instead of a ROI, Equation (4) is the

calculation of the global NPS, assuming that the image noise is wide-sense stationary. However, CT image noise on a global scale violates this assumption of wide-sense stationary noise; therefore the estimation of the NPS in CT images should be calculated locally. The three-dimensional (3D) local NPS for volumetric CT can be calculated for any ROI $\mathbf{g}'$ within an image as below:

$$NPS(f_i) = \frac{v_x v_y v_z}{N_x N_y N_z} \langle |\mathbf{DFT}\{\mathbf{g}'_\mathbf{i} - \bar{\mathbf{g}}'_\mathbf{i}\}|^2 \rangle \tag{5}$$

Here, the NPS is scaled proportionally to the CT voxel dimensions in millimeters (v_x, v_y, v_z) and inversely proportional to the number of ROI voxels in each dimension (N_x, N_y, N_z) in order to compare spectrums calculated from images with varying voxel dimensions and ROI sizes. A multi-dimensional Fourier transform can be performed on volumetric images to obtain a NPS with the same dimensionality. For a more convenient visual representation of the 3D NPS, the two-dimensional (2D) central transverse slice (i.e. where $f_z = 0$) is usually extracted, from which a one-dimensional (1D) radial profile is generated. In this study, the 2D central transverse slice will be computed via the synthesized slice method, in which averaging is performed on a set of 2D noise power spectrums:

$$NPS(f_i) = \frac{p_x p_y}{N_x N_y} \Lambda_z \langle |\mathbf{DFT}\{\mathbf{g}'_\mathbf{i} - \bar{\mathbf{g}}'_\mathbf{i}\}|^2 \rangle_{N_{ROI}} \tag{6}$$

Here N_{ROI} is the number of 2D spectrums utilized for averaging. Pixel dimensions (p_x, p_y) are substituted here for voxel dimensions to denote a 2D process. The factor Λ_z is related to the length over which the spectrums are averaged. Since Λ_z has units of length, the NPS in both Eq. 2 and Eq. 3 will have dimensions of

variance multiplied by volume, in this case HU^2 mm^3, where HU stands for CT Hounsfield numbers. By utilizing the radial symmetry of the 2D NPS, a 1D spectrum can be generated by binning the data according to its radial spatial frequency, followed by averaging the data in each bin.

A.3.2. Modulation Transfer Function

The MTF can be calculated from acquired images of an sharp-edged object. First, the edge spread function (ESF) of the edge to-be-analyzed must be obtained. For a known edge position, the ESF is obtained by binning the image pixel data according to their distance from the edge. The derivative of the ESF is performed to obtain the line spread function (LSF), and applying the discrete Fourier transform to the LSF yields the MTF:[12]

$$MTF = \mathbf{DFT}\{\frac{d}{dx}ESF(x)\} \tag{7}$$

The LSF is often normalized to have an area of unity prior to calculating the MTF, resulting in $MTF_{max} = 1$.

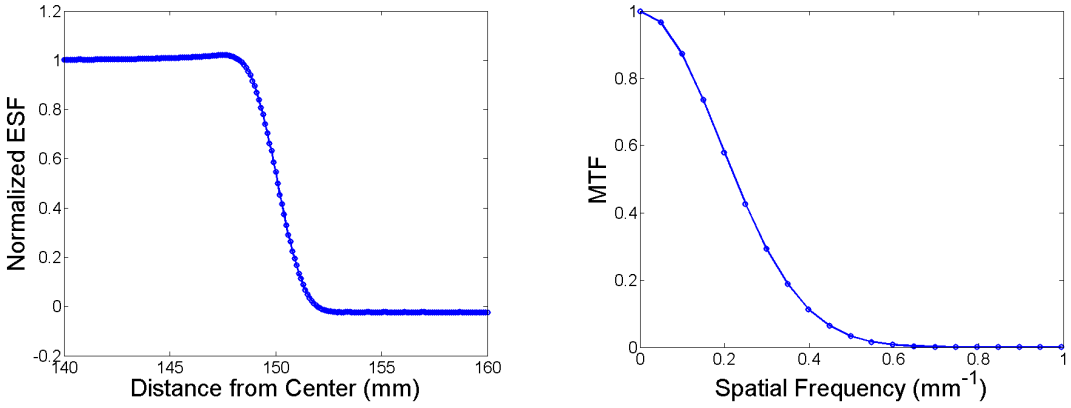

Figure 2. A measured ESF (left) with the corresponding calculated MTF (right).

The NPS and MTF improve upon the standard deviation and subjective line-pair test by providing a robust Fourier-based analysis in the frequency domain. These metrics are also practically ideal in that they are readily obtainable from acquired images. However, the calculation of the NPS and MTF presume specific imaging conditions that are not always strictly satisfied. More specifically, for NPS calculation image noise must wide-sense stationary, meaning that the image mean values must be constant across the entire image and the covariance of the image data must depend only on the relative position between image data points. For MTF calculation, images must be spatially invariant, meaning that the point spread function must be consistent across the entire image. These strict requirements are often not satisfied, particularly for modern CT imaging, which introduces some error into calculation of these metrics.[15] Moreover, these metrics in and of themselves do not correspond to intended clinical tasks.

B. Human Visual System (HVS) Based Metrics

In an attempt to objectively quantify image quality for human observers, many models have been developed based on the human visual system (HVS) from which IQA metrics can be calculated. These models most often assume that a reference or “gold standard” image can be obtained, and images are compared to this standard for similarity as interpreted by a simulated human observer.

These models are often utilized in the image processing community to adjust, optimize, and compare image quality, but have also been employed in medical imaging. This class of image quality algorithms will therefore be incorporated into this study and compared to the model observer for radiation therapy.

B.1. Structural Similarity Index

While there are many IQA metrics available that are based in HVS models, one of the most commonly used metrics today is the structural similarity (SSIM) index. A brief explanation will be given here; any additional desired information can be found in the appropriate reference.[6] The SSIM is the combination of three image components: luminance, contrast and structure. Given two images, where one is regarded as a “gold standard” image of perfect quality, the calculated SSIM describes the quality of the second image. First, the luminance, denoted as *l*, refers to the signal strength of the image pixels, and is defined using the image mean. Once the mean is subtracted from the image, the contrast component, *c*, is calculated using the standard deviation. The images are then each normalized by their own variance, and the final component, structure (*s*), is calculated. The SSIM is a weighted multiplication of the three components, resulting in a two-dimensional map of the quality difference between the two images:

$$SSIM(i,j) = [l(i,j)]^{\alpha}[c(i,j)]^{\beta}[s(i,j)]^{\gamma} \tag{8}$$

The weights α, β, and γ are chosen based on the desired importance of the individual components. It is often convenient to represent the SSIM as a singular scalar quantity by calculating the mean of the SSIM:

$$\mu_{SSIM} = \frac{1}{N_i N_j} \sum_{n_i=1}^{N_i} \sum_{n_j=1}^{N_j} SSIM(i_{n_i}, j_{n_j}) \tag{9}$$

Figure 3 shows an example of μ_{SSIM} calculated for distorted photographs compared to an original.

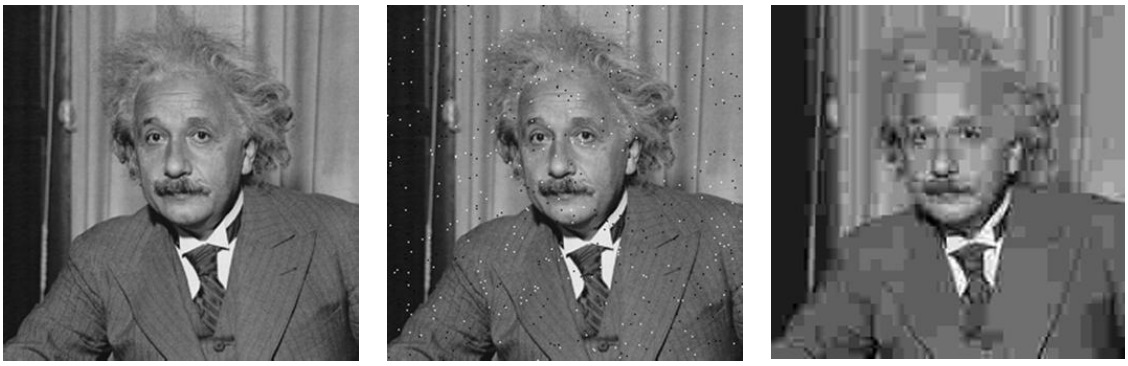

(a) MSE = 0, μ_{SSIM} = 1.000

(b) MSE = 144, μ_{SSIM} = 0.840

(c) MSE = 142, μ_{SSIM} = 0.662

Figure 3. Comparison of the mean SSIM for two distorted photographs compared to an original, which is viewed as the "gold standard". While the salt-and-pepper like noise in Figure 3b may result in a higher mean square error when compared to Figure 3c, the significant blurring in Figure 3c distorts the overall clarity of the structures in the image, resulting in a lower μ_{SSIM}. The images as well as the values for MSE and μ_{SSIM} were obtained from a reference website.[16]

Several other HVS models have been developed as well to assess image perceptual such as the Case-PDM,[7] Sarnoff's IDM (also known as the JND

model),[17] and DCTune (developed by NASA).[18] The HVS-based metrics provide quantitative metric for IQA which resembles a human observer but does not require the work hours of a human observer. Additionally, the subjectivity introduced by human observer IQA is also removed. However, there are limitations to using HVS-based models for IQA. First, images with fundamentally different pixel values (e.g. CT vs. MRI, T1-weighted vs. T2-weighted MRI) cannot be adequately compared, as the fundamental structural differences obscure the structural differences arising solely from image quality degradation.[7] Additionally, as with the physically-based metrics, correlation to clinical task performance is not direct and therefore these algorithms need to be compared to clinical task performance first prior to usage for IQA.

C. Task-Based Image Quality Assessment

Distinct from the previously mentioned IQA approaches, task-based image quality assessment objectively quantifies image quality based on the task that an observer will perform using the available images. The initial theories for task-based IQA were posited by Wagner *et al*.[19] for diagnostic imaging tasks. Task-based IQA is based in statistical decision theory, meaning that the observer makes use of all the available information when forming a decision. This includes the deterministic and stochastic properties of imaging systems, as well as the nature of the task itself. A robust theory for task-based IQA has been formulated

elsewhere for diagnostic imaging,[8, 9] but a brief summary is provided here in order to illustrate the application of task-based IQA theory.

C.1. Image System Modeling

To develop a framework for task-based image quality assessment, both the imaging system and the object to be imaged must first be known. A simple description of an image system is provided below:

$$\mathbf{g} = \mathbf{H}\mathbf{f} + \mathbf{n} \tag{10}$$

Here **f** is the object to-be-imaged, **H** is the imaging system, **g** is the final image, and **n** is noise introduced to the image from the imaging system. Thus the role of the imaging system is to map the object to the image, with noise added during the process. Under the assumption that **H** is linear and spatially invariant, the Fourier analysis of the deterministic properties of the imaging system is the modulation transfer function:

$$\mathbf{H} \xrightarrow{\mathcal{F}} MTF \tag{11}$$

Similarly, if the covariance of the noise vector $\mathbf{C_n}$ is calculated and the noise is wide-sense stationary, the Fourier analysis of the stochastic properties of the imaging system is the noise power spectrum:

$$\mathbf{C_n} \xrightarrow{\mathcal{F}} NPS \tag{12}$$

While the MTF and NPS can be calculated from **H** and $\mathbf{C_n}$, it is also possible to obtain them directly from acquired images as described in Section 2.A.

C.2. Task Definition

Secondly, the task to be performed on the image must be clearly defined. In diagnostic imaging, the task is most often a binary classification task, meaning that the observer must make one of two decisions: either the disease to-be-diagnosed is present or absent in a particular image. For this task type the disease signal presence is determined within the context of a background signal; either the disease signal is present or the image is background-only. For binary classification tasks additional information may or may not be known prior to the observer performing the task, such as the potential signal location and the signal-background image intensity difference.

C.3. Ideal Model Observer Derivation

Having defined the imaging system and the task to be performed, the next step in task-based IQA framework development is the description of observer performance, which ultimately yields the task-based IQA metric, the figure of merit (FOM). As an example the ideal or Bayesian observer will be derived. The ideal observer minimizes the risk when determining a decision strategy for a given task. In a binary classification task two possible hypotheses, denoted by h, exist: either the disease is absent (h_1) or present (h_2). The observer is given a set of images, again denoted by the discrete vector $\mathbf{g}$, and must decide which hypothesis is true of this particular image set. The observer performs this task by

choosing the most probable of the two hypotheses, given the ratio of posterior probabilities:

$$\frac{pr(h_2|\mathbf{g})}{pr(h_1|\mathbf{g})}, \tag{13}$$

where $pr(h_2|\mathbf{g})$ is the conditional probability of the disease being present given the images and $pr(h_1|\mathbf{g})$ is the conditional probability of the disease being absent given the images. Using Bayes theorem these probability distributions can be rewritten accordingly:

$$pr(h_n|\mathbf{g}) = \frac{pr(\mathbf{g}|h_n)pr(h_n)}{pr(\mathbf{g})}. \tag{14}$$

Substituting Eqn. 14 into Eqn. 13, the probability ratio can be expressed as a likelihood ratio L:

$$L = \frac{pr(\mathbf{g}|h_2)}{pr(\mathbf{g}|h_1)}. \tag{15}$$

Given the image data **g**, the ideal observer decides which hypothesis is true by comparison to a threshold L_C; $L > L_C$ would signify disease present and $L < L_C$ would signify disease absent. Thus the ideal observer minimizes the decision risk by choosing the most likely hypothesis for the acquired image data.

The simplest application of the ideal observer is when the location, shape, size, and image intensity for both the signal and background are known exactly, denoted as SKE/BKE. In this instance the only source of randomness in **g** is the image noise, and the image data can be completely characterized by its mean

and covariance. The ideal likelihood value can then be determined directly from the image data:

$$L_I = (\mathbf{H}\boldsymbol{\Delta}\mathbf{f})^t \mathbf{C}_\mathbf{n}^{-1}\mathbf{g}, \tag{16}$$

where *t* is the matrix transpose operator and **Δf** is the object difference between the two hypotheses. Having defined a likelihood ratio in terms of the imaging system properties, a figure of merit (FOM) can be derived. Given the nature of **g**, the ratio L_I will have a probabilistic distribution for each hypothesis. The distinguishability between these two probability distributions is the measure of how well an observer will be able to perform the binary classification task. The FOM for the ideal observer, the signal-to-noise ratio (SNR), can be calculated using the mean and variance of the L_I distributions:

$$SNR_I^2 = \frac{[\langle L_I \rangle_2 - \langle L_I \rangle_1]^2}{[\sigma_2^2 + \sigma_1^2]/2}. \tag{17}$$

Substituting Eqn. 16 into Eqn. 17 and performing simplification, the ideal observer SNR can be calculated using information of the imaging system and object:

$$SNR_I^2 = (\mathbf{H}\boldsymbol{\Delta}\mathbf{f})^t \mathbf{C}_\mathbf{n}^{-1}(\mathbf{H}\boldsymbol{\Delta}\mathbf{f}). \tag{18}$$

If the MTF and NPS can be obtained, either by using Eqns. 11 & 12 or from the methods described in Section 2.A., the ideal observer calculation can be rewritten in terms of Fourier-based metrics:

$$SNR_{Ideal}^2 = \int \frac{|\Delta\tilde{f}(\nu)|^2 MTF(\nu)^2}{NPS(\nu)} d\nu. \tag{19}$$

With the physical properties of the imaging system being conveniently summarized using the noise-equivalent quanta (NEQ):

$$NEQ(\nu) = \frac{MTF(\nu)^2}{NPS(\nu)} \tag{20}$$

Thus a FOM has been derived which directly quantifies observer performance for the task of diagnostic imaging, given the images and known information regarding the object and task.

C.4. Other Common Model Observers

In addition to the ideal or Bayesian observer, two other observers are commonly utilized within the diagnostic imaging community to accommodate for other sources of randomness besides image noise. First, if the disease signal position is only known statistically, then the Hotelling observer can be utilized:

$$SNR_{Hot}^2 = \int \frac{|\Delta\tilde{f}(\nu)|^2 MTF(\nu)^2}{MTF(\nu)^2 NPS_f(\nu) + NPS_n(\nu)} d\nu \tag{21}$$

The non-prewhitening matched filter is also used under similar conditions as the Hotelling, and has also shown to model human observers adequately:

$$SNR_{NPWMF}^2 = \frac{\left[\int |\Delta\tilde{f}(\nu)|^2 MTF(\nu)^2 d\nu\right]^2}{\int |\Delta\tilde{f}(\nu)|^2 MTF(\nu)^2 [MTF(\nu)^2 NPS_f(\nu) + NPS_n(\nu)] d\nu} \tag{22}$$

.

Thus for a variety of signal/background conditions there exists a model observer which assesses the image quality for a signal detection task and outputs a scalar figure of merit, the SNR.

D. Task-based IQA for Radiation Therapy: The TOC Curve

The vast majority of task-based image quality assessment has been focused on diagnostic imaging tasks, in particular the task type of binary classification. This task type is not suitable for radiation therapy, where the main objective is to treat the patient by maximizing the radiation dose to the tumor or disease while minimizing the dose to surrounding normal tissues. The work performed by Barrett *et al*.[10] was the first to provide theory for task-based image quality assessment in radiation therapy. The derivations relevant to the following model observer framework, including the TOC as the proposed FOM, will be summarized here, along with the distinctions between this referred work and the proposed dissertation project.

D.1. TOC Curve Concept

Radiation therapy treatments utilize images to delineate the tumor and any relevant structures near the tumor which may also receive radiation. The goal of treatment planning is then to deliver the required radiation dose to the tumor while minimizing the dose to normal tissues. The efficacy of radiation therapy treatments can be quantified statistically using the probability of tumor control, Pr(TC), and the probability of normal tissue complication, Pr(NTC). These

quantities are calculated using knowledge of the radiobiological interactions between the radiation and tissue cells, in conjunction with clinical trials in which actual patient outcomes are quantified. The plots of *Pr*(TC) and *Pr*(NTC) resemble a sigmoid-like shape as a function of radiation dose, as shown in Figure 4. These plots can be utilized to evaluate treatment efficacy by calculating the ratio between the two probabilities for a given dose, a quantity known as the *therapeutic ratio*. For example, in Figure 4 the treatment on the left is of higher quality than that on the right, as a higher tumor control can be achieved for the same normal tissue complication.

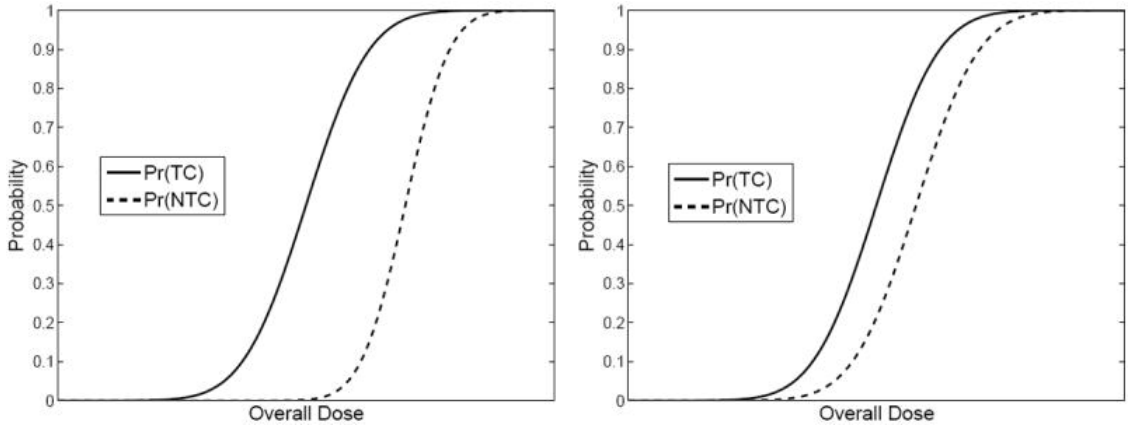

Figure 4. Sample plots of the tumor control probability and normal tissue complication probability for two different radiation therapy treatments. The left plot has a higher therapeutic ratio and is therefore considered a superior treatment. This figure was obtained directly from a reference.[10]

Given that these curves closely resemble the sensitivity and specificity plots of the ROC curve, a therapeutic operating characteristic (TOC) curve was proposed as the description of treatment efficacy. For the TOC curve, the normal

tissue complication is plotted on the abscissa while the tumor control probability is plotted on the ordinate. This enables the comparison of multiple treatments on the same figure. In addition, the area under the TOC curve (AUTOC) can be readily calculated and then used as a singular, scalar figure of merit. An example of TOC curves for the treatments in Figure 4 is shown in Figure 5. The dashed line in Figure 5 corresponds to the treatment plan on the left in Figure 4, and likewise the solid curve in Figure 5 corresponds to the treatment plan on the right in Figure 4. By quick comparison it can be seen that the treatment corresponding to the dashed line yields a higher AUTOC and is therefore a higher quality treatment plan.

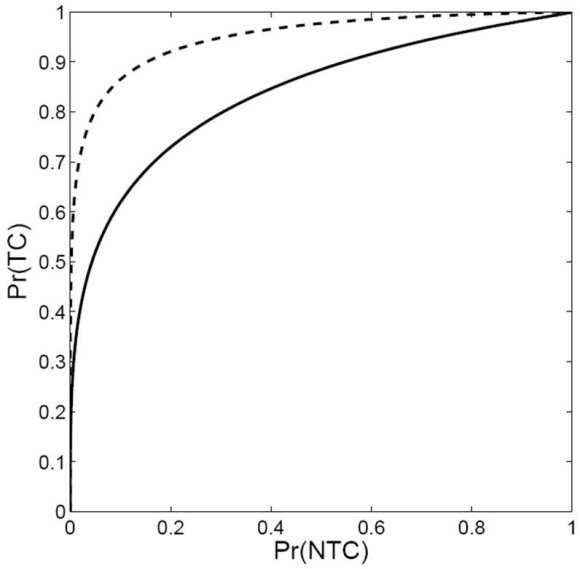

Figure 5. The therapeutic operating characteristic curves for the treatment plans in Figure 4. The dashed line corresponds to the treatment plan on the left, and the solid curve corresponds to the treatment plan on the right. This figure was obtained directly from a reference.[10]

D.2. TOC Curve Estimation

Having proposed the TOC curve and the AUTOC as the FOM, the next step is to find the relationship between the acquired images and the TOC curve.

Following the paradigm of diagnostic task-based IQA, images of a known object (i.e. patient) are first acquired. It is therefore assumed that the patient's tumor and normal organs have a clearly defined and known shape, denoted as **B**. Acquired images of the patient prior to treatment will be denoted as a discrete vector **G**. From these images the tumor and relevant normal tissue boundaries will be estimated and described as discrete surfaces, denoted by $\mathbf{B}_{est}$. From the images and estimated boundaries, an optimal treatment plan is designed which will result in a dose distribution **D**. This dose distribution can be represented as a scaling of a fractional dose $\alpha\mathbf{D}_0$. Thus α represents the abscissa of Figure 4, and is a hidden parameter in Figure 5. Thus choosing a value for α computes a particular point on the TOC curve, and the entire TOC curve is obtained by sweeping α across a relevant range of dose values.

In statistical decision theory, the observer makes use of all the available information, including the stochastic properties of the system. In this paradigm all sources of randomness are described as conditional probability density functions (PDFs), denoted by *pr*. In radiation therapy, the stochastic quantities that affect the *Pr*(*TC*) and *Pr*(*NTC*) are image noise, randomness in the estimated boundaries, uncertainty in the actual delivered dose distribution, and the stochastic nature of tissue response to radiation. All of these effects will be quantified using these conditional PDFs.

First, let $pr(\mathbf{G}_j \mid j)$ describe the variability of the patient's images due to image noise; the index *j* has been introduced to denote an individual patient.

Next, $pr(\mathbf{B}_{est,j} \mid \mathbf{G}_j)$ will be defined as the probability of estimating a certain set of boundaries given an image set. The PDF for the patient's optimized dose distribution given the estimated boundaries and images is $pr(\mathbf{D}_j \mid \mathbf{B}_{est,j}, \mathbf{G}_j, j)$. Finally, the probability of tumor control given the optimized dose distribution and the known, ground-truth organ boundaries is $Pr(TC \mid \mathbf{D}_j, \mathbf{B}_j, j)$. Note here that the known patient organ boundaries are used instead of the estimated boundaries for tumor control probability calculation, enabling a ground truth assessment. Given these definitions, the probability for tumor control can be defined as a combination of these PDFs:

$$Pr(TC|\alpha, j) = \iiint Pr(TC|\mathbf{D}_j, \mathbf{B}_j, j) pr(\mathbf{D}_j|\mathbf{B}_{est,j}, \mathbf{G}_j, j) \ldots pr(\mathbf{B}_{est,j}|\mathbf{G}_j) pr(\mathbf{G}_j) d\mathbf{D}_j d\mathbf{B}_{est,j} d\mathbf{G}_j \quad (23)$$

A similar equation can be derived for normal tissue complication probability:

$$Pr(NTC|\alpha, j) = \iiint Pr(NTC|\mathbf{D}_j, \mathbf{B}_j, j) pr(\mathbf{D}_j|\mathbf{B}_{est,j}, \mathbf{G}_j, j) \ldots pr(\mathbf{B}_{est,j}|\mathbf{G}_j) pr(\mathbf{G}_j) d\mathbf{D}_j d\mathbf{B}_{est,j} d\mathbf{G}_j \quad (24)$$

The TOC curve can then be plotted as a function of α, with Eqn. 24 as the x-axis and Eqn. 23 as the y-axis.

D.3. Simplification for External Beam Radiation Therapy

While this integral can be solved numerically, some simplifying assumptions will be made to improve the tractability of the integral. First, it is

assumed that the dose calculation process is non-random, i.e. that it will return the same dose distribution for a given image set and organ boundaries. Secondly, it is assumed that the patient-to-patient variation of the TCP is negligible, so that the variable *j* can be safely dropped from the first term. Finally, the last two terms are written as a joint probability: $pr(\mathbf{B}_{est,j} \mid \mathbf{G}_j)pr(\mathbf{G}_j \mid j) = pr(\mathbf{B}_{est,j},\mathbf{G}_j \mid j)$. Simplifying using these assumptions, and translating to a numerically solved integral, yields the following equation:

$$Pr(TC|\alpha) = \frac{1}{K}\sum_{k=1}^{K} Pr[TC|\mathbf{D}(\mathbf{B}_{est,k}, \mathbf{G}_k), \mathbf{B}] \tag{25}$$

The subscript *j* has been dropped for the sake of clarity, but Eqn. 25 still represents the tumor control probability for an individual patient. Thus the tumor control probability can be estimated averaging a simulation of imaging, organ delineation, dose calculation, and outcome modeling over many (*K*) iterations for the same patient. The AUTOC can be used to optimize image quality for one patient, or the numerical integration in Eqn. 25 can be repeated for many patients to optimize an imaging device for a population of patients.

The paramount contribution of the reference by Barrett *et al*. is the introduction of the AUTOC as a figure of merit for radiation therapy. In addition, within this reference suggested applications are proposed for image segmentation, patient motion, and molecular imaging, with corresponding derivations and simplifications of *Pr*(*TC*) and *Pr*(*NTC*). However, the proposed

methodology is prefaced on manual segmentation of clinical images as the known, ground truth for patient data.[10, 11] Moreover, to the best of our knowledge none of the proposed methodologies have been previously implemented. It is therefore the purpose of this dissertation to fill in the gap by providing a robust, fully-computer-simulated model observer capable of task-based IQA for radiation therapy.

CHAPTER 3: A MODEL OBSERVER FOR TASK-BASED IQA IN RADIATION THERAPY

Having described the foundation for task-based image quality assessment in radiation therapy, the design for the proposed model observer is presented, which will objectively assess images for the task of radiation therapy. Strategies and guidelines pertaining to the development of the fully-computer-simulated model observer will be outlined in this chapter. The general and specific details of the model observer are described in Sections A and B, respectively. Section C outlines details regarding the specific radiation therapy task utilized in this study, and Section D concludes the chapter by providing the programming ideology for the software development of the computer-simulation model observer.

A. Model Observer General Strategy

The general strategy of the radiation therapy model observer is to use all the available images acquired of a specific patient to design and deliver an optimal radiation therapy treatment to the patient. This optimal plan is then assessed for patient treatment efficacy. Figure 6 describes this general strategy by depicting a flowchart of the inputs and output of the model observer. Following the paradigm of task-based IQA, the object that is being imaged must be known. Therefore the object model, which contains the actual organ boundaries of the patient using geometric surfaces, is included as one of the inputs to the model

observer. CT images of the object model are generated, a process which will be fully described in Chapter 4, and these images to-be-assessed are also included as input. Finally, the treatment prescription input includes information regarding the task of radiation therapy, such as the prescription dose to the target, the dose constraints for the at-risk normal tissues, and specific details of the treatment modality (IMRT, brachytherapy, etc.). The model observer uses these three information inputs to plan and evaluate the patient's treatment. The output of the model observer is the figure of merit, a singular scalar value which objectively quantifies image quality for the task of fulfilling the radiation therapy treatment prescription.

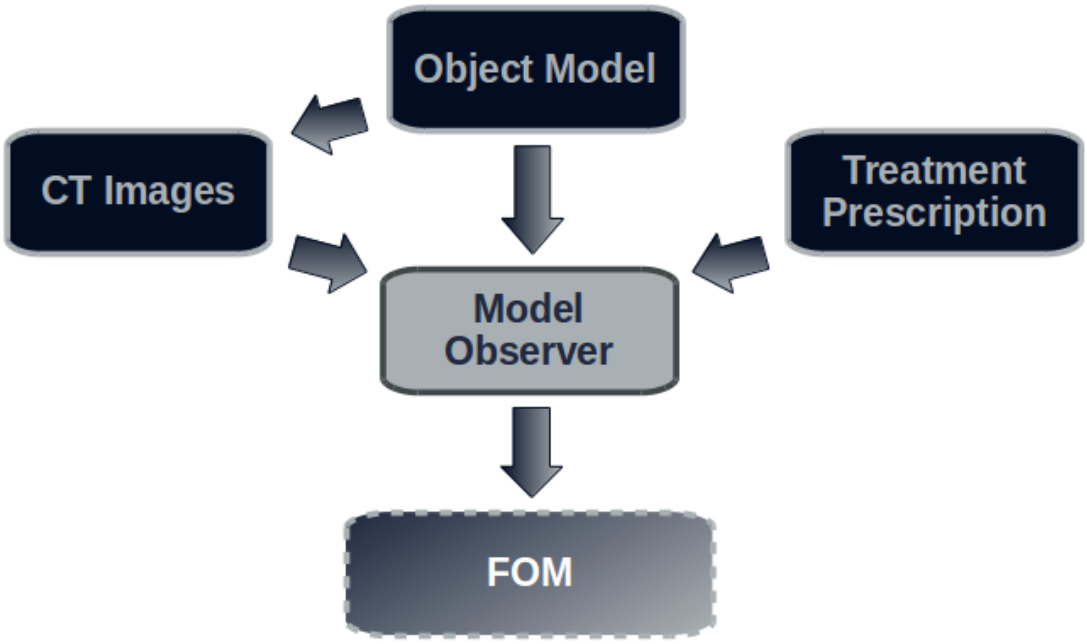

Figure 6. The generalized strategy design for the radiation therapy model observer. The known object, images of the object, and task information (i.e. treatment prescription) are used as system inputs. The model observer designs an optimal treatment plan, which is evaluated for efficacy, yielding the FOM.

B. Model Observer Implementation Schematics

As an initial implementation of the model observer, this study emulates a minimalistic radiation therapy treatment workflow. While many different imaging modalities are used for a variety of purposes (see Section 1.B.), only the initially acquired CT images will be considered for this study. Thus treatment planning is performed with only the CT images, and no image guidance in included. Consequently, neither patient motion nor patient setup errors are considered, and it is therefore assumed that the delivered dose is equal to the planned dose. Given these constraints, the goal of this study is to optimize the IQA of these initially acquired CT images (also known as simulation CT images) for the task of treating the patient.

The specific steps of the model observer implementation is depicted in Figure 7. A fully-computer-simulated framework will be developed to resemble a model observer for radiation therapy by simulating an end-to-end radiation therapy treatment. The CT images are segmented semi-automatically to obtain the estimated tumor and normal tissue boundaries; these images and estimated boundaries are used to design and deliver an optimal dose distribution. Finally, the optimized dose distribution is evaluated in terms of patient treatment outcome, using the known patient treatment boundaries and radiobiological modeling. For this study the AUTOC as proposed by Barrett *et al.* will be utilized as the FOM. Note that the model observer does not use the ground-truth object

model boundaries to plan the patient's treatment, but rather the CT images and estimated boundaries are used for planning. The object model is only utilized at post-treatment for evaluation by computing the patient outcome via radiobiological modeling. Chapter 5 provides a detailed description of the model observer implementation.

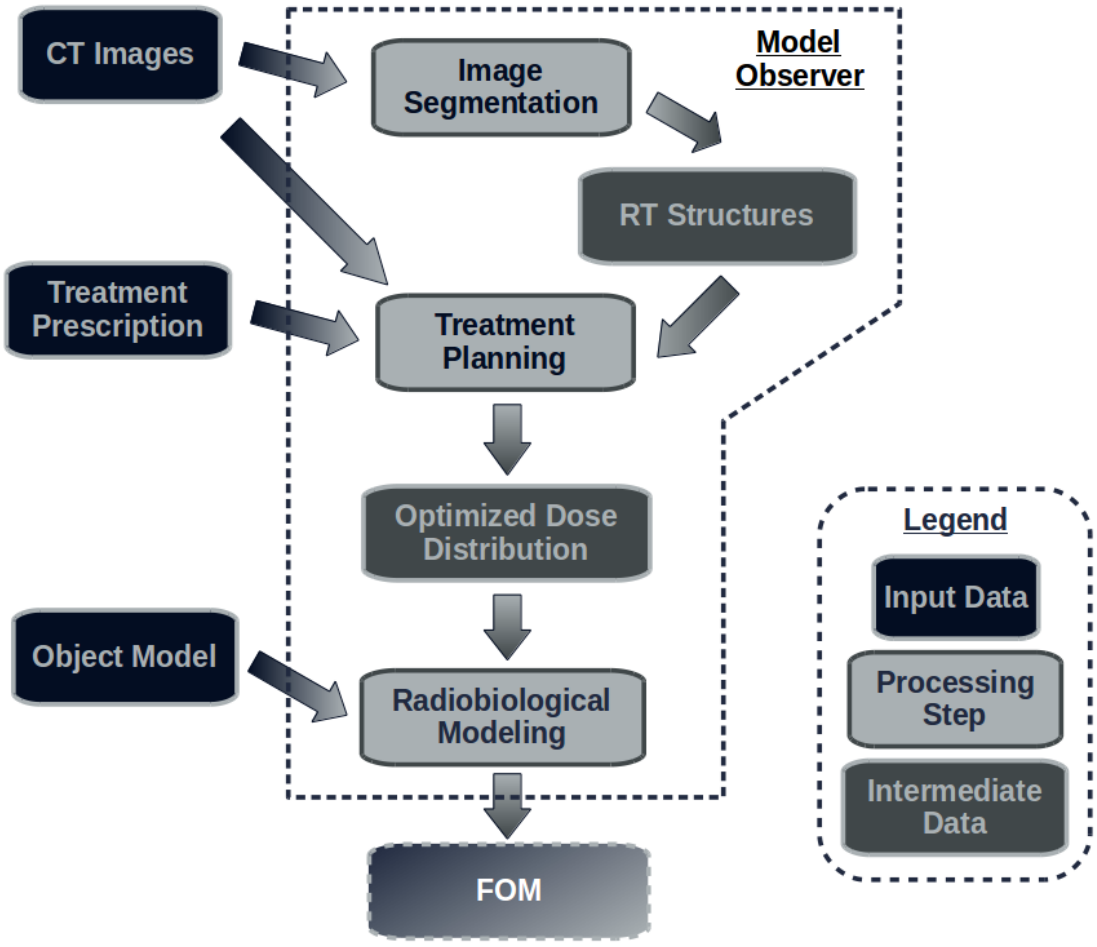

Figure 7. The specific framework design of the radiation therapy model observer.

C. Treatment Site & Modality Selection

For initial implementation, the specific radiation therapy task of an intensity-modulated radiation therapy (IMRT) treatment for prostate cancer was chosen. This is due to the readily available contours of the prostate a the target of radiation, and the relative ease of treatment planning and delivery as an established modality. Thus in Chapter 4, male pelvis numerical phantoms are specifically generated for use in this study. Similarly, all treatment plan details in Chapter 5 assume an IMRT treatment. Dose prescriptions and constraints for a prostate IMRT treatment were obtained from a literature review and included within the treatment prescription.

D. Programming Ideology

In order to feasibly utilize this computer-simulation model observer for radiation therapy, the software should be automated, with minimal user interaction. In addition, as the end-to-end radiation therapy treatment consists of many intermediate steps, integration of these individual components into a unified model observer is necessary for automation. While some software tools exist for treatment planning and radiobiological modeling, these tools rely heavily on user input. In addition, these tools are written using various programming languages, further hindering automation and integration. Moreover, some of the aforementioned applications do not allow for flexibility in parameter control for the different aspects of the treatment. Therefore, most of the software source code

was written as a part of this dissertation project. Following the object-oriented approach to programming, each step of the process was treated as an encapsulated object, responsible either for storing data or for mapping data, as shown in Figure 7. In order to have flexibility in parameter control for the different aspects of the treatment, many of the encapsulated objects were written specifically for this project. Given the large number of repetitive calculations required for such a framework, the C++ programming language was chosen for all self-written code for increased performance. This also enables the usage of many useful libraries (e.g. ITK, FFTW, and OpenMP). Any other packages written in a different programming language were incorporated by writing a C++ wrapper class as an abstraction to the packaged code.

In this chapter, the general strategy and programming approach were described for the newly proposed model observer. The model observer uses the object, images, and task information as inputs to design and deliver a radiation therapy treatment plan. The plan design is performed via computer simulation, with each step in the treatment process constructed as an encapsulated object as per the object-oriented programming paradigm. This plan is subsequently evaluated in terms of patient treatment outcome, which is conveniently summarized using the FOM. A prostate IMRT treatment was chosen for specific implementation in this study.

CHAPTER 4: SIMULATING REALISTIC IMAGES OF KNOWN OBJECTS

As a part of the simulation framework mentioned in the previous chapter, which follows a task-based IQA paradigm, the object that is being imaged must be known. This chapter therefore describes the detailed implementation of creating realistic images of a known object model. A persistent challenge for the quality assessment of radiation therapy treatments (e.g. contouring accuracy) is the absence of the known, ground truth for patient data. Moreover, assessment results are often patient-dependent, as treatment plans are patient-specific. While several numerical phantoms exist which can be used for simulation imaging studies,[20–23] previously reported numerical phantoms do not include the statistical properties of inter-patient variations, as their models are based on only one patient. In addition, these models do not incorporate tumor data. Therefore, a new methodology was developed for generating numerical phantoms which encapsulate the statistical variations of patients within radiation therapy, including tumors. In addition, this methodology enables an adequate assessment of image quality by incorporating a large patient population, as stated in Section D.3. of Chapter 2.

This chapter begins by providing the methodology for organ modeling, which utilizes inter- and intra-structural geometric attribute distribution (GAD) models. These models provide the mechanism to estimate both the deterministic

and stochastic properties of patients within radiation therapy. Next, a description is provided of how to generate realistic helical CT projection data of the newly created object model. Finally, the details of the filtered backprojection algorithm utilized to obtain the CT images is described in detail.

A. Object Modeling Using GAD Models

In order to ensure realism of the object being imaged, the organs within the object must be geometrically realistic in terms of inter-structural (e.g. organ-to-organ distance) and intra-structural (e.g. shape, size) properties. In addition, in order for the organ variations to be statistically relevant, the organ stochastic properties must be based on actual patient data. Thus the methodology of generated organ models is based on a scalable and deformable geometric attribute distribution (GAD) models that were trained using existing radiotherapy contours, which were originally employed to automatically detect contouring errors.[24]

As shown in Figure 8, the proposed realistic numerical phantom generation methodology includes two phases: GAD model training and numerical phantom generation. In the model-training phase, a number of patient cases with approved contours are utilized as the training sets to build the GAD models. GAD models were employed to model the shape and position of each relevant organ. Given a sufficient data set of *M* patients with *N* contour samples per organ per patient, a model can be trained to estimate both the deterministic and stochastic

properties of these organs using principal component analysis (PCA). The general strategy of the GAD model training is as follows: 1) determine the mean and covariance of each attribute (i.e. shape and centroid), 2) apply PCA to determine most significant components of randomness.

Then the numerical phantoms representing varied human anatomy structures can be generated using the GAD models by applying randomized but statistically sound weights to the principle components obtained by the model training. First, randomized shapes for each organ are generated using the shape GAD model. A centroid for each organ is then generated using the centroid GAD model, and the organ shapes are then positioned accordingly. To perform the imaging simulation, the numerical phantom is exported as a set of triangular meshes, one for each organ in the phantom. Therefore mesh creation, in addition to final post-processing, is performed to finalize the numerical phantom. A statistically relevant ensemble of numerical phantoms can be generated by using a new set of randomized weights for each new phantom.

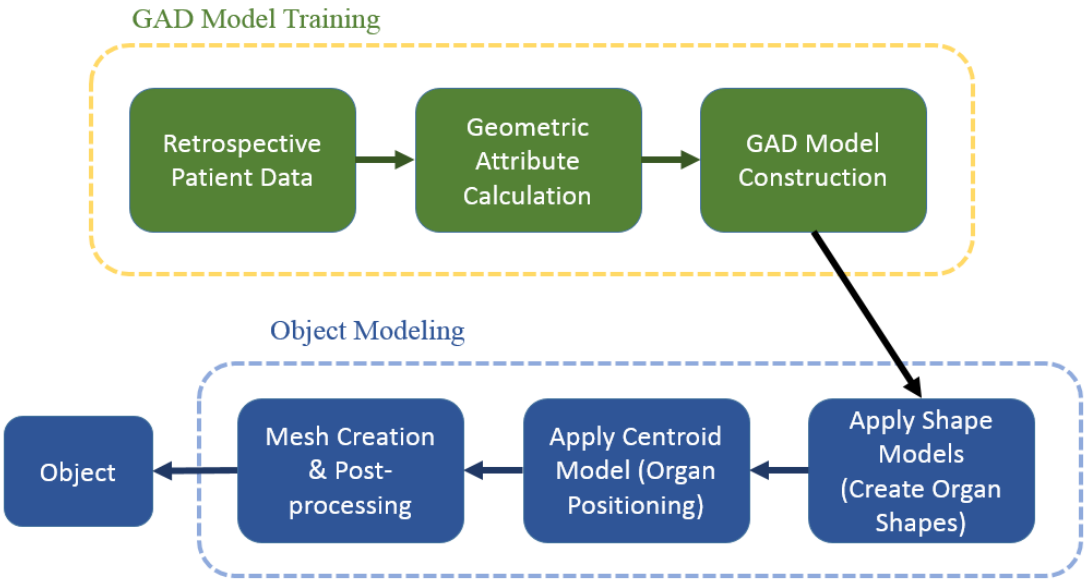

Figure 8. The proposed methodology for generating realistic objects using inter- and intra-structural GAD models.

A.1. Inter-Structural Centroid Modeling Theory

For a given set of organ centroids $c_{m,n}(x,y,z)$ for the mth patient and n^{th} organ, the mean and covariance of an organ centroid are calculated using the following equations:

$$\bar{c}_n = \frac{1}{M}\sum_{m=1}^{M} c_{m,n}, \quad COV_{c_n} = (\bar{c}_n - \mathbf{c}_n)^T(\bar{c}_n - \mathbf{c}_n). \tag{26, 27}$$

Here **c** is a vector containing all centroids for a particular organ and *T* is the transpose operator. By performing singular value decomposition (SVD) on *COV* a vector of covariance eigenvalues $\boldsymbol{E}_n$ can be obtained defining the principle components of the centroid variation. By assigning a weighting factor to each

component of $\boldsymbol{E}_n$, the combination of mean centroid and weighted $\boldsymbol{E}_n$ can represent a new centroid attribute $\boldsymbol{C}_n$:

$$\mathbf{C}_n \approx \bar{c}_n + \mathbf{E}_n \mathbf{B}_n, \tag{28}$$

where $\boldsymbol{B}_n$ is the weight vector.

A.2. Intra-Structural Shape Modeling Theory

Organ shapes were modeled using implicit surfaces.[25, 26] To effectively compute the shape attributes of segmented organs from a CT image, which can be large, a 3D local cuboid region that contains the segmented organ was first determined. Then the shape attribute of the nth organ segmentation of the mth patient training set can be represented using a signed distance function, based on the distance from the hth point within the cuboid, $\boldsymbol{p}_h$, to the segmented organ surface:

$$\mathbf{\Psi}_{m,n}(\mathbf{p}_h) = \begin{cases} -dis(\mathbf{p}_h),\ if\ \mathbf{p}_h\ is\ outside\ surface \\ 0,\ if\ \mathbf{p}_h\ is\ on\ surface \\ dis(\mathbf{p}_h),\ if\ \mathbf{p}_h\ is\ inside\ surface \end{cases}, \tag{29}$$

where *dis* is the shortest Euclidean distance between the $\boldsymbol{p}_h$ and the surface. The mean and covariance of each organ shape model is obtained in a similar manner as the centroid model (Eqns. 26 and 27). After application of PCA to the shape covariance a vector of eigenvalues $\boldsymbol{U}_n$ is obtained defining the principle components of shape variation. Applying a weight vector $\boldsymbol{A}_n$ to the eigenvalues produces a generalized shape model:

$$\mathbf{\Psi}_n \approx \bar{\Psi}_n + \mathbf{U}_n \mathbf{A}_n. \tag{30}$$

Thus once the centroid and shape GAD models have been generated, the weight vectors $\boldsymbol{B}_n$ and $\boldsymbol{A}_n$ can be altered for each component to produce random organ shapes. Thus it is possible to generate organs with random shape and position, and this randomness represents the variety of patients typically seen in the clinic, as defined by the training dataset.

A.3. Training Data Set Acquisition

For this study, the archived retrospective patient data sets from our institution were semi-automatically searched to locate 20 prostate patient cases. Data was transferred using the FTP protocol via open-source FileZilla software,[27] and information was extracted from the TAR-extension archived files using LibArchive.[28] A MATLAB GUI was developed to extract the segmented structures from the patient datasets, and then to subsequently view and export the patient's RT structures, as shown in Figure 9. All relevant RT structures to a prostate IMRT treatment including the prostate, bladder, rectum, femoral heads, and seminal vesicles were utilized. In addition, the patient's external contour and was also utilized. The male pelvic bones can significantly affect CT image quality, but the pelvic bones are typically not segmented within a prostate patient case. Therefore the archived patient database was searched again and three pelvic bone structures from patient cases were located and utilized for shape/centroid modeling. These structures were exported individually and stored in a database for organ modeling.

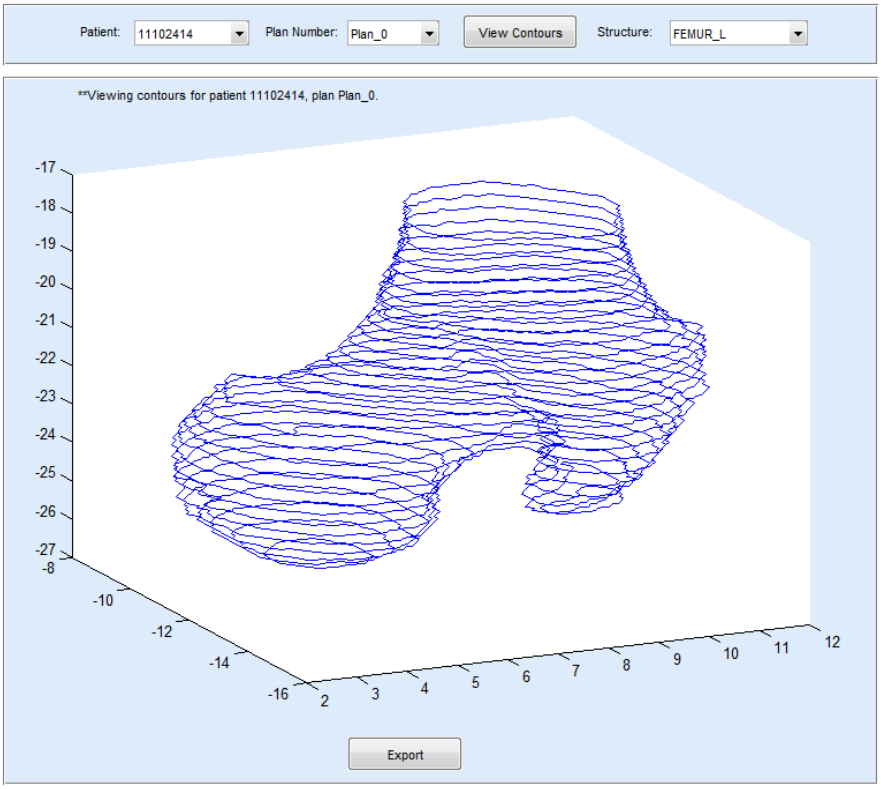

Figure 9. The MATLAB software for semi-automatic searching and extraction of retrospective patient data.

A.4. GAD Model Training and Organ Generation

These exported structures were utilized to train the GAD models using the aforementioned methodology. Prior to training the centroid models for each organ, Procrustes analysis was utilized to minimize the pose differences (i.e. scale, orientation, and position) among the training contour sets for accurate centroid attribute distribution analysis.[29] Similarly, for shape modeling all the exported structures were first translated so that their centroid was located at the origin, to facilitate an unbiased analysis. After training the GAD models for

centroid and shape, new organ shapes and centroids are generated from the models by using randomized but statistically sound parameter weights. Given the nature of the implicit surfaces defined by Eqns. 29 and 30, the newly generated shapes are also represented as signed distance functions. A simple thresholding technique is performed to produce a binary image; voxels in the cuboid region values greater than or equal to 0 are assigned a value of 1, indicating that they belong to the structure. The structure surface was then obtained by calculating the perimeter of the binary image. Figure 10 depicts a two-dimensional slice of the signed distance function and the corresponding thresholded image, with the perimeter contour superimposed in blue. The contour points generated from this process were exported as a three-dimensional point cloud.

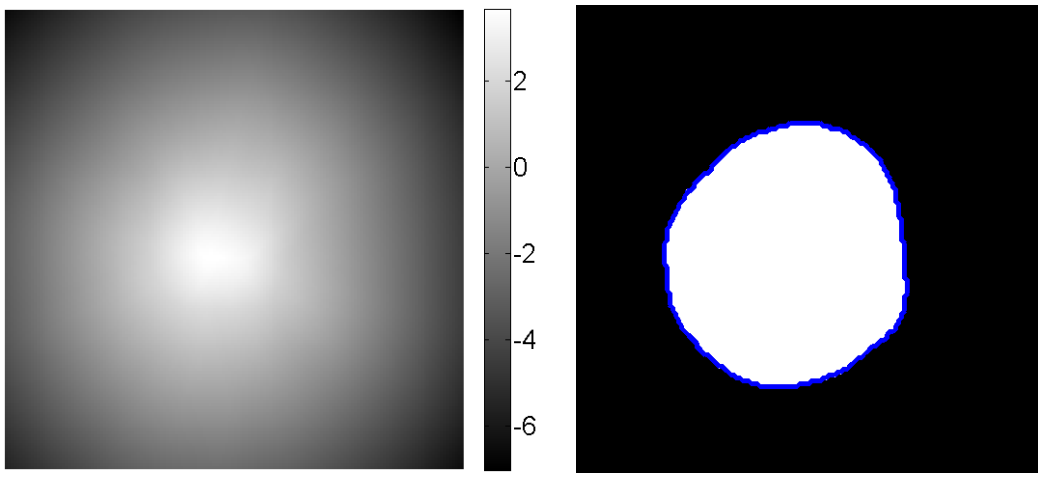

Figure 10. A two-dimensional slice of the signed distance function (left) and the results after thresholding and perimeter determination (right).

The point cloud is then transferred to the open-source MeshLab software[30] for processing. First, the point normals for the point cloud are calculated, then the

a triangular mesh is created from the point set using Poisson surface reconstruction.[31] The meshes are simplified using quadric edge collapse decimation[32] and Taubin smoothing[33] to increase calculation speed of the projection data. Figure 11 displays an organ surface created for a femoral head, processed using the Meshlab software.

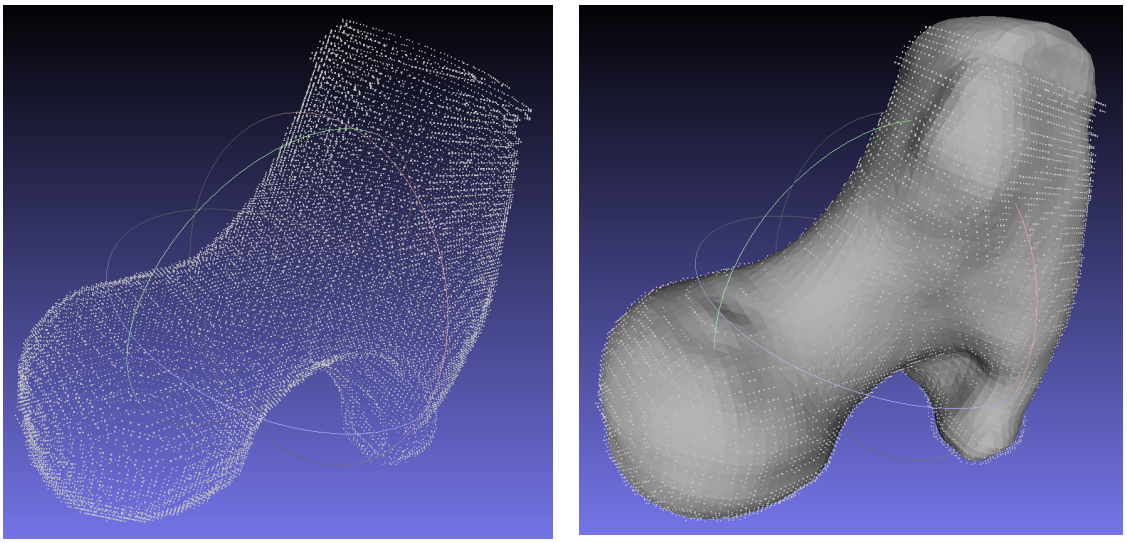

Figure 11. The exported RT structure, the left femoral head, as a point cloud (left) and as a triangular mesh (right) after Poisson surface reconstruction.

A.5. Object Model Creation

Finally, to create an object model of a patient, all the generated structures are translated to their newly generated centroid. The MeshLab software was used to remove any structure overlaps present. To facilitate the calculation of CT projection data, the generated structures are incorporated into a hierarchical tree structure, which captures the parent-child relationship between each structure

and the world. Figure 12 displays a sample hierarchical tree structure. For each object model, shapes and centroids were generated using the GAD models for bladder, prostate, rectum, femoral heads, pelvic bones, and the patient's external, and each tissue was assigned a tissue material type from the NIST database, as explained in the following section. In addition, for the three bony structures (femurs and pelvis) an interior layer triangular mesh was created to accommodate for the lower-density cancellous bone. This was performed by scaling the exterior layer mesh by 1.5 mm, in the direction of the vertex normals of the exterior mesh, to create a new interior mesh.

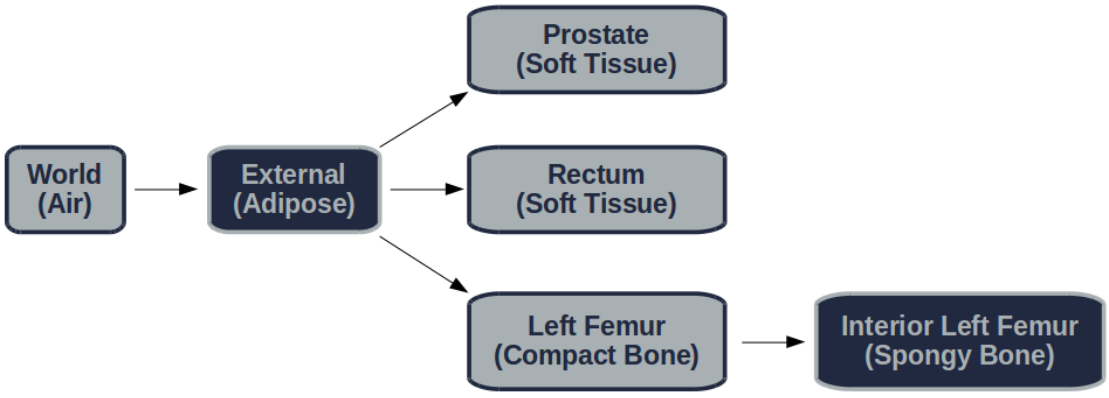

Figure 12. An example of the hierarchal tree used to place organs relationally.

B. CT Projection Generation Using Exponential Attenuation

In order to generate CT images of an object model, projection images were first simulated by tracing a ray from the source through the object model to each detector element, and calculating the resulting intensity using exponential attenuation:

$$I(d) = \sum_{i=1}^{N_e} I_0(E_i) e^{(-\sum_{n=1}^{N_s} \mu(E_i) l_n)} \tag{31}$$

The imaging source spectrum $I_0(E)$ was generated by implementing the TASMIP algorithm,[34] resulting in a spectrum sampled at integer kVp intervals from 1-150 kV. Each structure was assigned a specific material (e.g. air, soft tissue, bone, etc.), and a C++ class was developed to load and calculate linear attenuation coefficients (μ) that were obtained directly from the NIST database online.[35] Table 1 lists the utilized materials for this study and the corresponding structures for each material. NIST data was not available for spongy bone; cortical bone was used as a substitute, with a decreased density applied. Logarithmic interpolation was utilized to obtain values for each energy of the source spectrum.

Material Name	**NIST Material**	**ρ (g/cm^3)**	**Structures**
Air	Air, Dry	0.001205	World
Adipose	Adipose Tissue (ICRU 44)	0.95	External
Bone (Compact)	Bone, Cortical (ICRU 44)	1.92	Femurs (Exterior)
Bone (Spongy)	Bone, Cortical (ICRU 44)	1.0	Femurs (Interior)
Soft Tissue	Tissue, Soft (ICRU Four-Component)	1.0	Bladder, Prostate, Rectum

Table 1. The NIST materials utilized for the patient object models.

The calculation of path lengths l_n was performed using knowledge of the hierarchical tree structure as described in the previous section and depicted in Figure 12. For each source ray, the intersection length for the highest level (in this case the external contour) was calculated first, then the intersection lengths for the next sub-level (e.g. prostate), and so forth. The calculated path lengths for children were subtracted from the calculated parent pathlength to yield the correct ray path length through each organ structure. Then the appropriate attenuation coefficient was used in Eqn. 31 for the given photon energy and organ material. Since the organ models were represented as triangular meshes, the ray-triangle intersections between the source ray and the organ model needed to be calculated to determine the pathlength; this was performed using the highly optimized Möller-Trumbore algorithm.[36]

Prior to image reconstruction, Poisson noise is added to the projection images using the detector intensity, variable $I(d)$ from Eqn. 31, and a pseudo-random number generator. Therefore when using this model of CT projection generation the number of initial photons I_0, in addition to the magnitude of object attenuation, determined the amount of image noise in the projection domain. Finally, to complete the projection data calculation a Gaussian blur filter was applied to the projection data to simulate the degraded spatial resolution from signal spread within CT detectors.

A third-generation CT scanner was emulated to image the object model. Specifically, the physical properties of the Philips Brilliance 64-slice CT scanner

used in our clinic were used for modeling. Thus the scanner diameter was set as 80 cm, and the fan detector contained 672 channels for 64 detector rows, with dimensions of 1.0 and 0.625 mm, respectively. This yielded a maximum scan field of view of approximately 60 cm. Helically-acquired projection data was obtained by translating the source in the z-direction between projection acquisitions, with a helical pitch of 1.0. The acquired projection data was saved to text data files for image reconstruction.

C. CT Image Reconstruction Using Filtered Backprojection

To accommodate for the multi-slice, helically-acquired projection data, a filtered interpolation approach in the z-dimension was utilized to obtain single-slice, axial projection data. The filtered interpolation approach imitates the work of Taguchi and Aradate,[37] which is divided into two steps: 1) resampling by linear interpolation using adjacent data points; and 2) filtering the resampled data set. These axial slices were then reconstructed using a standard filtered backprojection (FBP) approach for fan-beam data.[38]

C.1. Projection Z-Filtering

Given the initial helically acquired projection data $p_i(\beta,\gamma,z)$, the aim of filtered interpolation is to sample a single axial slice of projection data $p(\beta,\gamma)$ that will be reconstructed using a traditional axial FBP technique. Projection resampling is performed first to obtain a set of values for each β and γ in the axial data set. These values span the range of the slice thickness, determined by the

user-defined filter width (*FW*), at uniformly spaced intervals. The resampled projections p_r are calculated via linear interpolation, with the weights *w* being determined by the z-position of the initial projections:

$$p_r(\beta,\gamma,i) = w(\beta,\gamma,j(i)) \times p_i(\beta,\gamma,j(i)+1) + (1 - w(\beta,\gamma,j(i))) \times p_i(\beta,\gamma,j(i)),$$

$$w(\beta,\gamma,j(i)) = \frac{z_r(i) - z_i(\beta,\gamma,j(i))}{z_i(\beta,\gamma,j(i)+1) - z_i(\beta,\gamma,j(i))}, \tag{32}$$

$$z_r(i) = z_0 + i \times \Delta z,$$

$$\Delta z = \frac{FW}{2 \times I + 1},$$

The desired number of interpolated points, determined by the parameter *I*, is also manually selected. Both the 180° and 360° complementary projection data are incorporated for data interpolation. Having obtained a resampled set of projection values for each *β* and *γ*, singular values for each axial projection data element are calculated by applying a user-defined filter:

$$p(\beta,\gamma) = \frac{\sum_{i=-I}^{I} w_f(i) \times p_r(\beta,\gamma,i)}{\sum_{i=-I}^{I} w_f(i)}, \tag{33}$$

where the filter design is determined by the weights $w_f(i)$.

C.2. Filtered Backprojection

The sampled axial projection data set is then reconstructed using a traditional FBP approach. Due to the fan beam acquisition, the back-projection was first weighted according to the scanner radius *D* and the projection channel angle *γ*:

$$p'(\beta,\gamma) = p(\beta,\gamma) \times D \times cos(\gamma), \tag{34}$$

Projection images are then filtered with a Fourier-domain based filter which is applied prior to backprojection. For our study an adjustable sinc filter was utilized, given by the following equation:

$$f(\omega) = \left|\frac{2}{a} sin\left(\frac{a\omega}{2}\right)\right| \quad for \quad -\pi \leq \omega \leq \pi \tag{35}$$

Here *a* is the adjustable parameter that allows for a trade-off between image sharpness and image noise: as *a* increases, the image noise decreases but so does the image sharpness. Figure 13 displays the effect of the parameter *a* on filtered projection data.

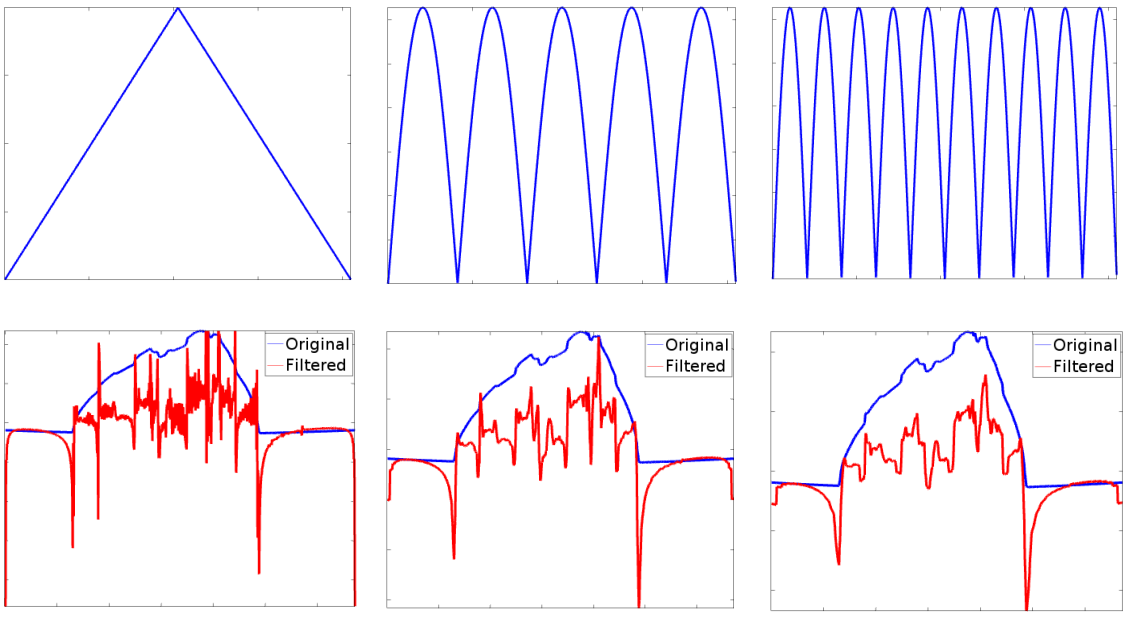

a ≈ 0 a = 5 a = 10

Figure 13. The adjustable reconstruction filter for different values of *a*. The top row displays the filter shape in the Fourier domain, while the bottom row displays a sample filtered projection the given parameter value. Note that as the adjustable parameter a increases the projection is smoothed and noise decreases, at the expense of degraded spatial resolution.

The filter is then applied to the weighted projection data at each source angle, denoted by $P'(\beta)$:

$$P_f(\beta) = \alpha \times IFFT\{FFT\{P'(\beta)\} \times f(\omega)\}, \tag{36}$$

Finally, the axial CT image pixel values $f(x,y)$ at pixel position (x,y) is calculated using a weighted backprojection of the filtered projection data p_f:

$$f(x,y) = \frac{2\pi}{M} \sum_{m=1}^{M} \frac{p_f(\beta_m, \gamma'(r,\theta,\beta_m))}{L^2(r,\theta,\beta_m)},$$

$$L^2(r,\theta,\beta_m) = [D + rsin(\beta_m - \theta)]^2 + [rcos(\beta_m - \theta)]^2, \tag{37}$$

$$\gamma'(r,\theta,\beta_m) = \frac{rcos(\beta_m - \theta)}{D + rsin(\beta_m - \theta)}.$$

Here M is the number of axial projections and r and θ are the polar coordinate equivalents of the pixel Cartesian coordinates x and y, with the origin located in the center of the reconstructed image space. Linear interpolation was utilized to sample $p_f(\beta,\gamma')$ from $P_f(\beta)$, which is only available for $-\gamma_m < \gamma < \gamma_m$ at intervals of α.

C.3. Implementation Details

All images in this study were reconstructed using the aforementioned approach, with FW = 3 mm and I = 4. For this project a rectangular filter was employed for the z-filtering (i.e. constant w_f for all values of i). Lookup tables for L^2, γ', and projection data z-positions were calculated prior to reconstruction to speed up computational time. All Fourier transform operations were executed using FFTW,[39] an optimized C++ library for fast Fourier transform calculation.

After reconstruction all images were saved with DICOM formatting using the ITK C++ library.[40]

D. Results & Discussion

Figure 14 depicts the results for the GAD centroid model. The left figure displays all the centroids utilized in this study, after performing Procrustes analysis. The Procrustes analysis proved effective in minimizing pose differences, enabling an unbiased statistical analysis of the centroid distributions. The right figure displays the statistical variation of centroids for the femoral heads, prostate, and rectum. The distributions are plotted as ellipsoids, with the three semi-principal axis lengths determined from the PCA results such that the ellipsoids contain 95% of the centroid variation in all three dimensions. Since the centroid model is trained while utilizing the aligned centroids from every organ, the inter-structural centroid differences are preserved.

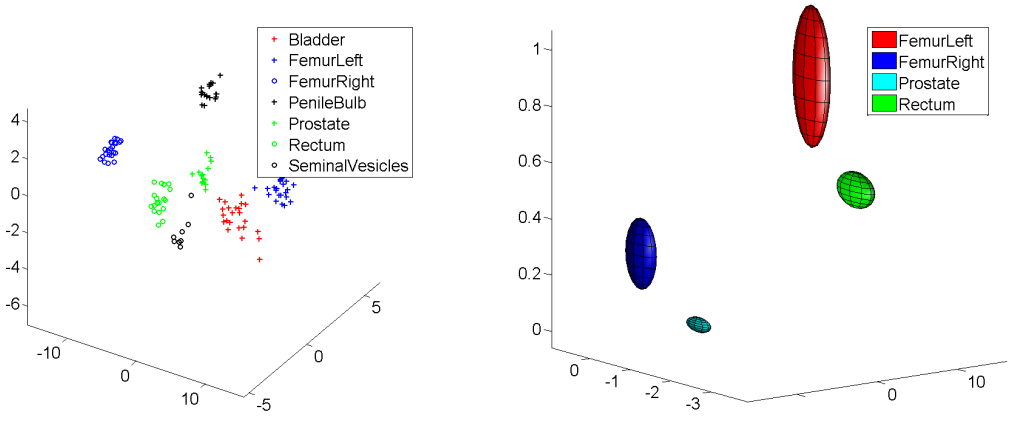

Figure 14. The results for the inter-structural GAD centroid model training. distribution of centroids for each organ in the training data set.

Figure 15 displays the results of the intra-structural shape GAD model training. Specifically, the mean shape is depicted alongside two simulated organs for the bladder (top row) and left femoral head (bottom row). New organ shapes can be generated by simply adjusting the GAD shape model weights in Eqn. 30. Note that two significantly different shapes can be generated using the same model, and both are incorporated into the statistical distribution of observed patients within the GAD model training data set. As expected, there is much more inter-structural shape variations for deformable tissues such as the bladder when compared to more rigid tissues such as the left femur bone.

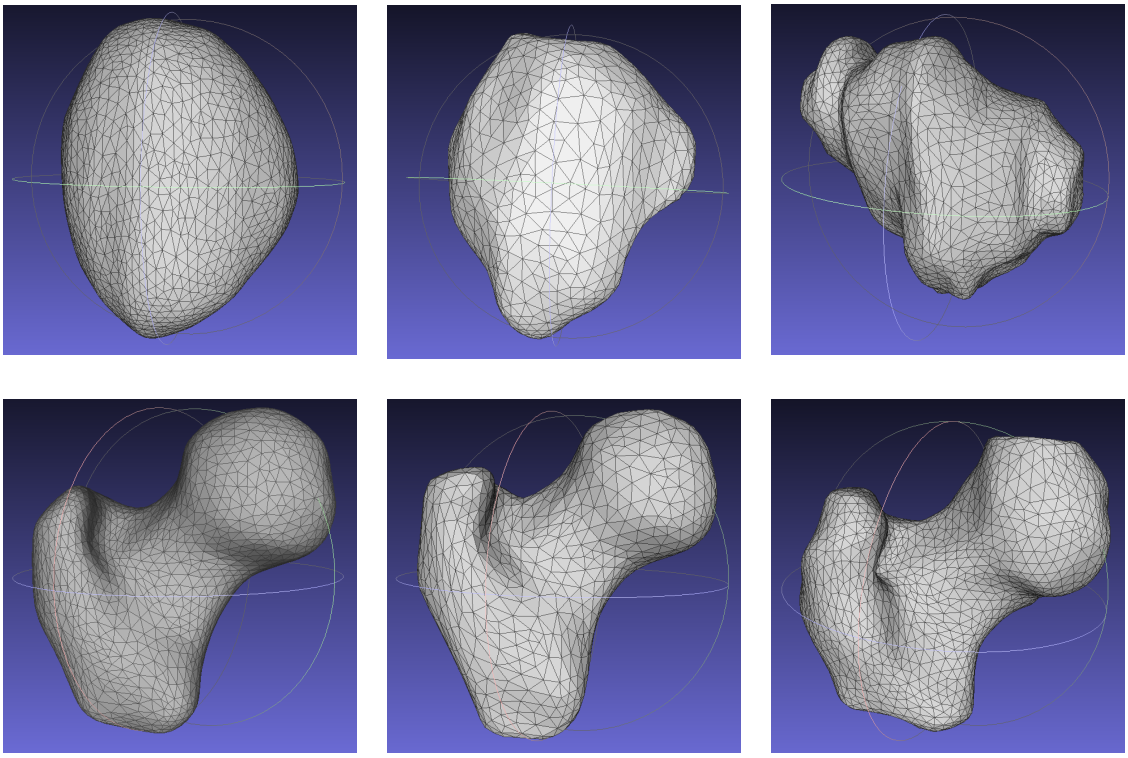

Figure 15. The results for the intra-structural GAD shape model training. The mean organ shape (left) and two simulated organs produced using the GAD shape model (center & right). The top row displays variations of the bladder, while the bottom row displays variations of the left femoral head.

Likewise, Figure 16 displays the final object model creation for two sample pelvis phantoms, demonstrating the positioning of the organs using the centroid model.

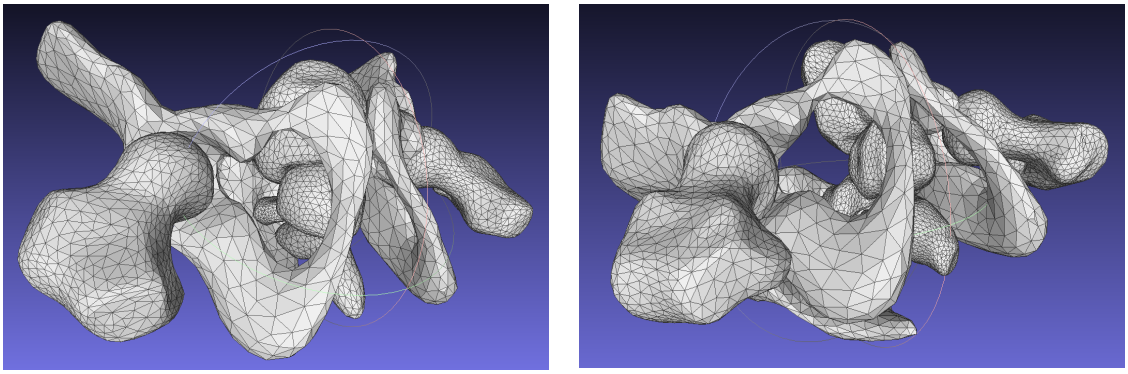

Figure 16. Two samples of generated patient objects. All organ models are pictured here, with the exception of the patient external contour.

Figure 17 displays various CT images generated using the object model and the process described in Sections B and C. As expected, when the imaging dose (i.e. number of photons per detector) and/or the filter parameter *a* increases, the imaging noise decreases. Also, as the number of photons increase the image contrast improves, as seen by the improved prostate-rectum separation when comparing Figure 17a-17c. However, when *a* is increased there is also an observable loss in spatial resolution, as seen by the blurred bone structures in Figure 17f when compared to Figure 17d. Since no beam hardening corrections were performed on the data, there are observable beam hardening artifacts, seen most clearly in Figure 17c.

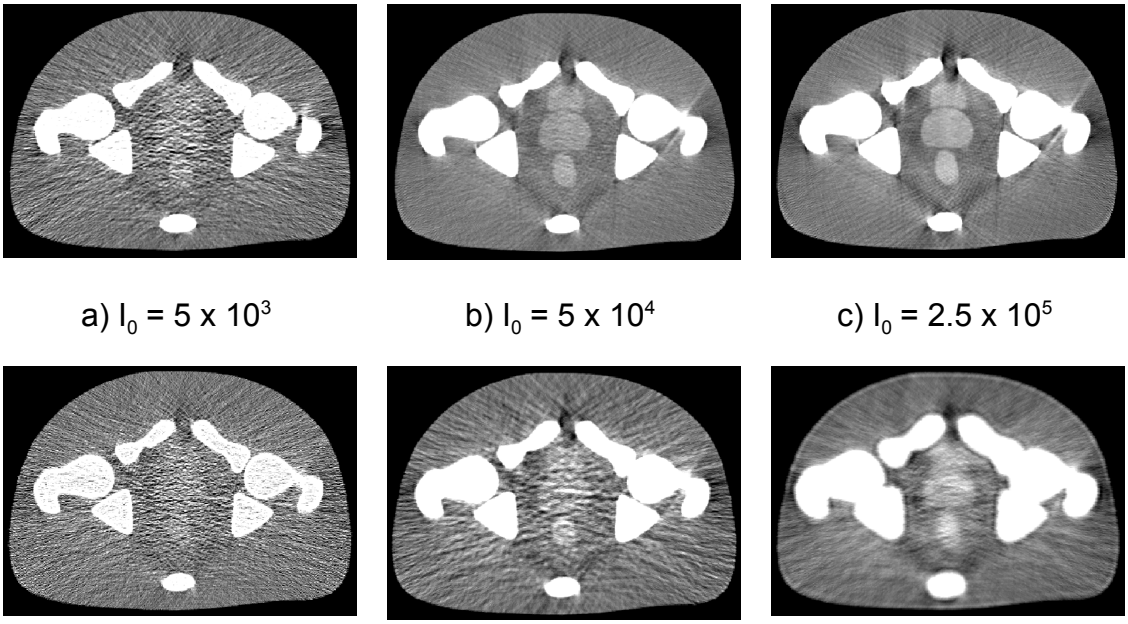

a) $I_0 = 5 \times 10^3$ b) $I_0 = 5 \times 10^4$ c) $I_0 = 2.5 \times 10^5$

d) $a \approx 0$ e) $a = 4$ f) $a = 10$

Figure 17. Simulated CT images for varying photon numbers and reconstruction filters. All images were generated using a 140 kVp source spectrum. The top row (a-c) was generated using the same filter parameter value (a = 2) and displays the decrease in noise as the number of photons increases. The bottom row (d-f) was generated using the same photon number ($I_0 = 5 \times 10^3$) and displays the decrease in noise and increase in spatial blurring as the filter parameter a increases.

In this chapter, realistic images were created of a known object. A methodology to generate a statistical ensemble of numerical phantoms was developed to create a population of patient objects. Both the stochastic and deterministic properties of these phantoms were based on retrospective radiation therapy patient data. CT projections could be obtained from an object via ray-tracing and exponential attenuation calculation. The adjustable parameter I_0 in Eqn. 31 determines both the amount of projection noise and the imaging dose.

These projections were reconstructed using a traditional FBP algorithm, with accommodation for helical projection data. An adjustable Fourier-domain based filter was employed, parameterized by the variable *a* in Eqn. 35, which controls both the noise and spatial blurring in the image domain. Both I_0 and *a* will be optimized for the task of radiation therapy in Chapter 6, after a detailed description of the model observer implementation in the next chapter.

CHAPTER 5: SIMULATION FRAMEWORK IMPLEMENTATION

Having obtained realistic CT images of a known object model, the next chapter proceeds to describe in detail the implementation of the model observer. Given these CT images, the model observer will first simulate an end-to-end radiation therapy treatment, including image segmentation (Section A) and treatment planning (Section B), which produces an optimized dose distribution. Then, having completed the treatment, the model observer will evaluate the treatment plan by estimating the tumor control and normal tissue complication probabilities for the optimized treatment dose using the ground-truth object model organ boundaries (Section C). These values for TCP and NTCP are conveniently summarized using the AUTOC, which is the FOM for this implementation of the radiation therapy model observer.

A. Semi-Automatic Image Segmentation Using ITK-SNAP

The first step in radiation therapy treatment planning is the segmentation (or contouring) of the target and potential organs at risk. Contouring can be performed either manually by a human observer, automatically by a computerized algorithm, or a combination of the two. It is known that manual segmentation by human observers is prone to subjectivity and randomness. This occurs mainly in two different aspects. First, the same human observer can delineate the same structure differently in each iteration. Secondly, two different

human observers will likely have two different average contours. However, automatic segmentation can be unreliable and often requires human supervision. To avoid contouring randomness while still ensuring human supervision, semi-automatic segmentation will be utilized for framework implementation.

Semi-automatic segmentation was performed with the open-source ITK-SNAP software. ITK-SNAP is a software application used to segment structures in 3D medical images.[41] ITK-SNAP provides semi-automatic segmentation using active contour methods, as well as manual delineation and image navigation. The latest version of the software can be downloaded freely from the appropriate website (http://www.itksnap.org/pmwiki/pmwiki.php). Segmentation in ITK-SNAP is comprised of two main steps: 1) Generation of a pre-segmentation "speed image", and 2) segmentation using geodesic active contours.

A.1. Pre-Segmentation Image Generation

The CT images acquired as described in Chapter 4, which are written and saved using DICOM formatting, are first imported into the software. Using the image navigation features a three-dimensional rectangular prism ROI is selected manually which encloses the organ to-be-segmented. Prior to application of the active contour method, a pre-segmentation "speed image" is created, with values in the range -1 to 1. The goal of pre-segmentation is to make the speed values close to 1 inside of the structure of interest, and close to -1 for other parts of the

image. Figure 18 shows an example of ROI selection and a pre-segmentation image.

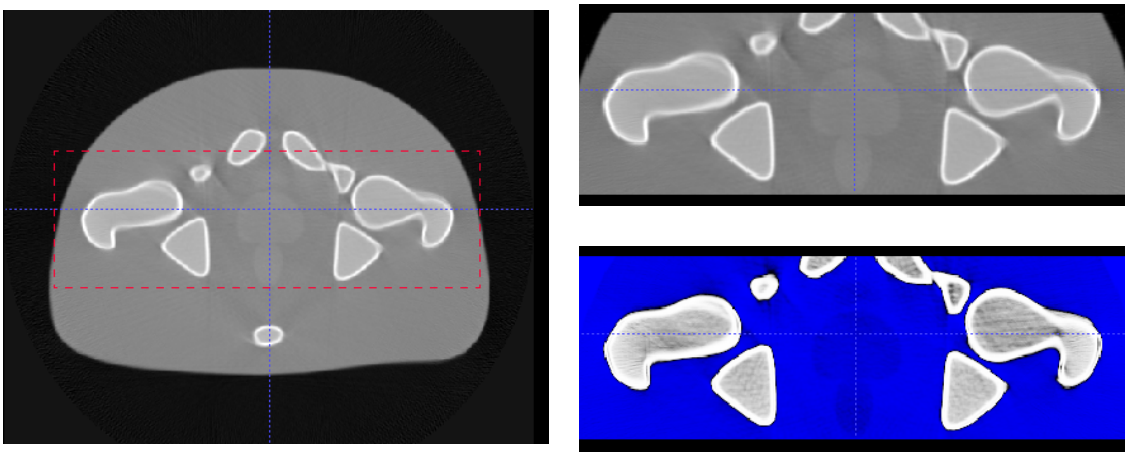

Figure 18. The process of creating a pre-segmentation “speed image” using ITK-SNAP. Regarding the speed image color map, the colors white, black, and blue correspond to the values 1, 0, and -1, respectively.

ITK-SNAP provides four methods for obtaining the pre-segmentation image: thresholding, classification, clustering, and edge-attraction. For thresholding, voxels with intensity inside of a user-specified range are mapped to positive speed values. Classification applies a machine-learning algorithm to segment images, utilizing manually drawn examples of tissue classes in the image. The clustering method automatically partitions the image into two or more tissue classes by clustering voxels with similar intensities together. Finally, the edge attraction method finds and emphasizes edges in the image. After manual inspection of all four methods, the thresholding method was selected as the most reliable for segmenting these particular CT images. In order to maintain

consistency between datasets, the same thresholding parameters were utilized for each image, which are listed in Table 2.

Tissue	$\text{Threshold}_{\text{min}}$ (CT #)	$\text{Threshold}_{\text{max}}$ (CT #)	$N_{\text{iterations}}$
Bladder	135	220	850
Femur	350	1550	600
Prostate	120	220	250
Rectum	120	220	200

Table 2. The parameter values for threshold-based region growing segmentation.

A.2. Geodesic Active Contour Algorithm

Segmentation is performed using a geodesic active contour algorithm, as proposed by Caselles *et al*.[42] The flow (i.e. growth) over time *t* of a contour *C* from an initial seed is proportional to the contour's normal by a force *F*:

$$\frac{\partial C}{\partial t} = F\vec{\mathbf{n}}. \tag{38}$$

The force *F* is of the form:

$$F = \alpha g_I + \beta\kappa + \gamma(\nabla g_I \cdot \vec{\mathbf{n}}), \tag{39}$$

where g_I is the speed function obtained from the values of the pre-segmentation image and κ is the mean curvature of the contour. The parameters α, β, γ are user defined. Intuitively, α affects the contour growth speed while β determines the smoothness of the contour's curvature. The third term is referred to as the

advection force and acts inwardly when the contour approaches speed image edges; in many applications a simplified version is chosen which ignores this force (i.e. $\gamma = 0$). For this application the simplified version was chosen, with values of 0.75, 0.75, and 0 selected for parameters α, β, and γ, respectively. In addition to these adjustable parameters, the user can also select the number of iterations (i.e. the length of time t) for the segmentation algorithm. To maintain consistency, organ-specific values for the number of iterations were chosen and held constant for all image sets; these values are also listed in Table 2. Once the segmentation has been performed, the segmented structures are exported as triangular meshes for treatment planning and dose calculation.

B. Treatment Planning

Treatment planning is divided into three steps. First, the plan is initialized by determining the placement of treatment beam angles and isocenter, in addition to the dose optimization constraints. IMRT beamlet initialization is also performed during this this step. Next, the initial dose to the patient with uniform beamlet weights is calculated using a Monte Carlo dose calculation engine. Finally, the beamlet weights are optimized to satisfy the previously defined dose constraints using a simulated annealing algorithm.

B.1. Treatment Plan Initialization

An IMRT prostate treatment plan was implemented, with parameters determined by literature review.[43] Five nearly-equiangular beams were utilized, at

beam angles of 35°, 100°, 180°, 270°, and 325°. All beams were directed at a common treatment isocenter, with a source-axis-distance of 100 cm. Given the design of the dose calculation software (as explained in the next section), only a static MLC delivery technique could be implemented. As such, each beam was split into a grid of 20 x 20 square beamlets, each beamlet having a side size of 1 cm at the isocenter plane. The centroid of the segmented prostate triangular mesh was chosen as the treatment isocenter; this enabled automatic isocenter calculation without user input. Dose-volume constraints used to optimize the dose distribution are summarized in Table 3. As stated in Chapter 3, no setup errors or patient motion was incorporated into the initial design; therefore no PTV margin was added to the initial segmented prostate.

Tissue	**Dose Constraints**			
	Type	**Value**	**Type**	**Value**
Bladder	$V_{70\ Gy}$	30%	$V_{55\ Gy}$	50%
Femur	$V_{50\ Gy}$	5%	-	-
Prostate	Min	78 Gy	Max	81 Gy
Rectum	$V_{70\ Gy}$	20%	$V_{50\ Gy}$	50%

Table 3. The dose constraints for the treatment plan.

Prior to dose calculation, each beamlet was checked to determine whether or not it passed through the target (i.e. prostate). This was accomplished by first determining which voxels in the CT dataset belonged to the prostate triangular

mesh. Then for each beam angle a ray was traced from treatment source, a point source located 100 cm away from the treatment isocenter at the appropriate beam angle. The intersection of this ray with the isocenter plane was calculated and subsequently checked to see if the intersection point belonged to any of the defined beamlets within the plane. Any beamlets which included these intersection points were marked as open. This process was repeated for each voxel point within the segmented prostate. The beam angle, isocenter, dose constraints, and open beamlet information were transferred as inputs to the dose calculation software.

B.2. Dose Calculation

The open-source Monte Carlo dose calculation engine Dose Planning Machine[44] (DPM) was utilized for the initial dose calculation, in order to achieve an accurate dose calculation. The source code for the FORTRAN-based software package can be downloaded directly from the web (https://inte.upc.edu/downloads). The base source code package is designed to calculate the absorbed dose delivered to a voxelized CT image dataset from a single square beam of x-ray radiation, given the beam size, location, and energy, in addition to the CT number to material composition conversion and a rectangular prism ROI within which to calculate the dose.

The package was adjusted slightly in order to accommodate several beamlets in a static MLC IMRT treatment. For a given isocenter, beam angle, and beamlet number (i.e. 0-399) from the treatment plan, the adjusted DPM program

calculated the beamlet location relative to the CT dataset. The CT number to material conversion was performed using the knowledge of linear attenuation coefficients provided by the NIST database and the TASMIP-generated CT source energy spectrum. Six different material classifications were utilized: air, lung, adipose tissue, soft tissue, skeletal muscle, and cortical bone. These materials comprise a sufficient material set for Monte Carlo dose calculations,[45] and the composition and density for each of these material was already provided with the base DPM package. The rectangular prism ROI for dose calculation was determined by the maximum and minimum x, y, and z values of the beamlet path as it traversed the CT dataset.

A C++ wrapper class was developed to handle the input file creation and output file extraction for the DPM package, providing integration with the rest of the simulation tool. The source energy spectrum for a 20 MV photon beam was used for dose calculation as it was already provided with the software package. The number of photons per beamlet was set to 1.5×10^6. The dose to each CT voxel from each of the opened beamlets was calculated using DPM and then stored for optimization.

B.3. Dose Optimization

Once the dose to each CT voxel from each beamlet has been calculated using DPM, the aim of dose optimization is to determine the beamlet weight w_b for each beamlet b that yields an optimal dose distribution. Dose optimization was performed using a simulated annealing based algorithm.[46] First, an initial

cost function value f_0 is calculated using a quadratic cost function. Given a dose constraints C_n for the nth constraint and an ideal dose distribution $\mathbf{D}_{Ideal}$, as established from treatment planning, the cost f_i at any iteration i is calculated as a weighted sum over all N constraints:

$$f_i = \sum_{n=1}^{N} w_n \{C_n(\mathbf{D}_{Ideal}) - C_n(\mathbf{D}_i)\}^2 \quad . \tag{40}$$

The weights for each constraint w_n are chosen manually by the user, depending on the relative importance of each dose constraint. Constraints can be based on minimum dose, maximum dose, or by a point on the dose-volume histogram curve; the list of constraints is given in Table 3 (thus N = 7 for this study). The initial dose distribution $\mathbf{D}_0$ was calculated by summing the dose contributions d for each of the voxels with indices j from each individual beamlet, for all B beamlets:

$$\mathbf{D}_0 = \sum_{b=1}^{B} \sum_{v=1}^{V_b} w_b \times d_b(j_{v,b}) \quad . \tag{41}$$

The voxel indices $j_{v,b}$ and number of voxels V_b per beamlet were determined during the dose calculation step. Initially, all beamlet weights w_b are set equal to 1.

For each iteration of the optimization, a beamlet number b is selected at random and the beamlet weight w_b is adjusted by applying a “grain” g to a beamlet weight and then recalculating the dose. The grain g is consistent in magnitude, but with randomly chosen sign (i.e. positive or negative). Since the dose contribution from each beamlet is stored individually, the total dose

distribution is altered at each iteration by adding or subtracting the beamlet grain dose:

$$\mathbf{D}_{i+1} = \mathbf{D}_i \pm g \sum_{v=1}^{V} d_b(j_v) \quad . \tag{42}$$

After recalculating the dose distribution the cost function is re-evaluated and compared to the cost function value from the previous iteration. If the cost function decreases the grain is accepted and the new beamlet weight and dose distribution are carried into the next iteration. If the cost function increases, the beamlet acceptance is defined by a probability *P* that decreases as the number of successful (i.e. accepted beamlet alterations) iterations n_a increases, based on a Boltzmann simulated annealing cooling schedule:[47]

$$P = 2B \times \left(1 + exp\left\{\frac{log(n_a + 1)}{T_0}\right\}\right)^{-1} \quad . \tag{43}$$

The parameters *B* and T_0 are user-defined prior to optimization. The optimization terminates after a user-defined maximum number of successful iterations, n_{max}, is reached. This methodology allows for completely automated optimization without convergence on local minima, but introduces a source of randomness into FOM calculation, which will be addressed in Chapter 6.

Lookup tables containing the list of voxels belonging to each structure were calculated prior to performing the optimization, to increase the calculation speed of the dose constraints. To avoid unphysical beamlet weights, a grain was rejected if applying the grain lead to a negative beamlet weight, and a new grain

and beamlet were chosen. Values for g, B, T_0, and n_{max} were chosen as 0.1, 0.5, 1.0, and 1000, respectively, determined by manual tuning to produce adequate dose distributions while minimizing the calculation time. A simple viewing application was created using the OpenGL graphics API,[48] for easy viewing of the optimized dose distribution overlaid on the CT images. The final beamlet weights and optimized dose distribution are saved as text data files which are used to calculate the TOC curve and AUTOC.

C. Radiobiological Modeling

Having completed the end-to-end simulation of an external beam radiation therapy treatment, the final step for the model observer is to evaluate the treatment by estimating the patient treatment outcome, based on the optimized dose distribution and the known ground truth organ boundaries. Several models and metrics exist to evaluate the patient treatment outcome, many of which are based on the radiobiological interactions of ionizing radiation with the DNA of tissue cells.[49] One such radiobiological model, the equivalent uniform dose (EUD),[50] is defined by the equation below:

$$EUD = \left(\sum_{i=1}^{N} v_i D_i \right)^{1/a} \tag{44}$$

Given the EUD for an organ, the tumor control probability (TCP) and normal tissue complication probability (NTCP) can be calculated accordingly:[51]

$$TCP = \frac{1}{1 + \left(\frac{TCD_{50}}{EUD}\right)^{4\gamma_{50}}}, \qquad NTCP = \frac{1}{1 + \left(\frac{TD_{50}}{EUD}\right)^{4\gamma_{50}}} \tag{45, 46}$$

To calculate the TCP and NTCP for this study, values for the parameters *a*, TCD_{50}, TD_{50}, and γ_{50} for all relevant tissues were obtained from the literature,[52] and are reproduced in Table 4.

Tissue	Tissue Type	a	TD_{50} (Gy)	TCD_{50} (Gy)	γ_{50}
Prostate	Tumor	-10	-	28.34	1
Bladder	Normal	8.33	80	-	4
Rectum	Normal	2	80	-	4
Femur	Normal	4	65	-	4

Table 4. Radiobiological model parameter values for the EUD-based calculation of TCP and NTCP. These values were obtained from a reference.

To compute the TOC curve, EUD is scaled by the parameter α as described in Section 2.D. For each value of α, a new EUD, TCP, and NTCP are calculated, producing a new point on the TOC curve. The range of α values are chosen such that the TCP and NTCP are fully sampled in the range from 0.0001 to 0.9999. Numerical integration of the TOC curve using the trapezoid rule produces the AUTOC. Using this procedure an AUTOC value is calculated for each normal tissue compared to the target (i.e. prostate). To conveniently summarize these contributions, a cumulative AUTOC is introduced which is calculated as the product of individual organ AUTOC values for all N_s normal tissue structures:

$$AUTOC_{cumulative} = \prod_{n=1}^{N_s} AUTOC_n \tag{47}$$

Thus the patient treatment outcome, and thereby the assessment of image quality, can be succinctly summarized using the cumulative AUTOC.

D. Results & Discussion

The results presented here relate to the simulation framework of an end-to-end radiotherapy treatment; application of the entire model observer for radiation therapy IQA is the subject of Chapter 6. Figure 19 displays the OpenGL viewer for images and dose distributions, in addition to the dose-volume histograms for the optimized plan. The constructed dose optimization software using the simulated annealing algorithm was able to satisfy all the constraints defined during the treatment planning process, and is therefore a realistic and acceptable treatment plan in terms of dose constraints.

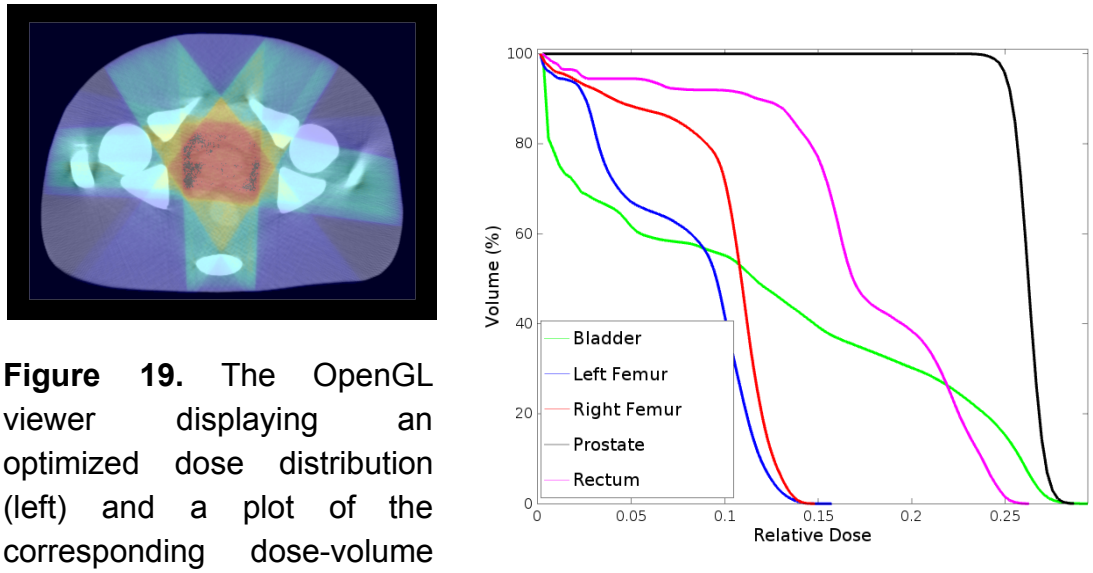

Figure 19. The OpenGL viewer displaying an optimized dose distribution (left) and a plot of the corresponding dose-volume histograms (right).

Figure 20 displays sample TCP, NTCP, and TOC curves calculated by the simulation framework. These curves are representative the typical TCP/NTCP/TOC curves calculated during this study. The choice of normal tissue complication in this instance is rectal bleeding, the most common adverse effect from radiation therapy of prostate cancer. Considering the realism of this treatment scenario, the therapeutic ratio (TCP/NTCP for a given α value) is much improved when compared to published works of clinical IMRT treatment plans.[53–55] This indicates that the current framework implementation presents a more idealized scenario than real clinical implementations. We hypothesize three main contributions to the decreased realism. First, since both patient motion and setup errors were not incorporated into this initial framework, no planning margin was added to the prostate; incorporation of a margin will certainly increase the dose to surrounding normal tissues and degrade treatment plan quality. Second, it was observed qualitatively that the image contrast between the soft tissues (prostate, rectum, and bladder) was enhanced when compared to clinically acquired images; this is a direct result of the choice of attenuation coefficients for Eqn. 31. Thirdly, no calibration to an actual linear accelerator was performed, and therefore no determination was made concerning the deliverability of the optimized treatment plan; it is possible that the optimized treatment plan in this study may not be deliverable. Finally, it was also observed qualitatively that the prostate-bladder-rectum organ spacing was greater than observed in clinical

images; this was in large part due to the method of organ intersection removal as described in Section 3.A. Many of these hypotheses can be tested and corrected by improved framework development. The magnitude of the effect of these four components on framework realism and AUTOC calculation will be investigated and improved as part of future work.

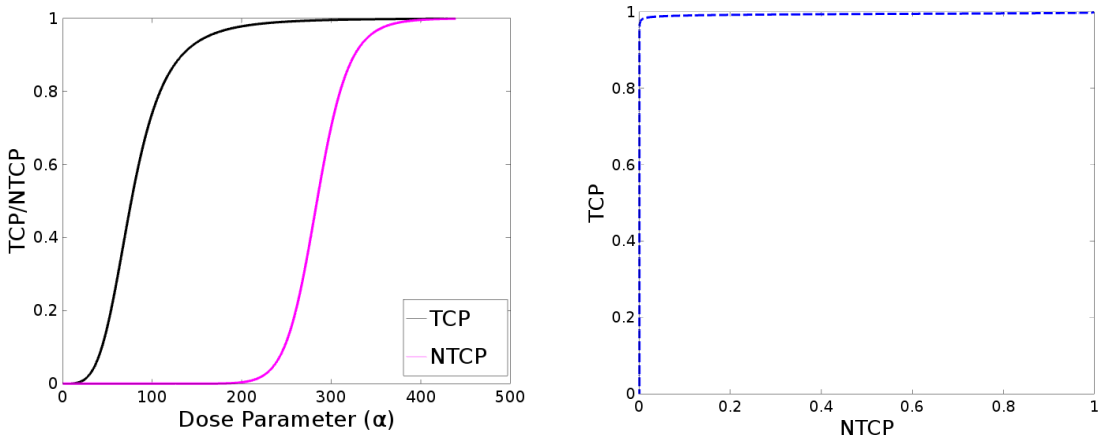

Figure 20. The TCP, NTCP, and TOC curves for prostate tumor control vs. rectal bleeding normal tissue complication, the AUTOC in this instance is 0.9929.

While some sources of bias will be addressed in Chapter 6, this study will not address the choice of segmentation parameters nor the choice treatment planning parameters. Both of these are active areas of research, with large bodies of literature associated with them.[56, 57] Optimization of these parameters are entirely separate projects, but it would be an interesting area of future research to evaluate and optimize these parameters in terms of the AUTOC.

In a related note, it is important to specify that the particular choice of parameters and algorithms for the end-to-end simulation are not guaranteed to

be ideally optimized for this particular patient or image dataset. For example, there are many state-of-the-art segmentation algorithms currently being applied within radiation therapy, such as atlas-based segmentation,[58, 59] which may improve segmentation performance compared to the results in this study. Similarly, this study does not propose to create a fully optimized treatment plan and delivery. Rather, the purpose of this study is to demonstrate image quality assessment using the proposed radiotherapy model observer. That is, for a given treatment plan, segmentation algorithm, treatment delivery machine, etc., the model observer provides a mechanism to objectively evaluate and optimize image quality, and image quality alone, for the task of radiation therapy. To evaluate one aspect of the treatment, all other parameters must be held constant.

In this chapter, an end-to-end simulation of an IMRT treatment for prostate cancer was implemented. Images were reliably segmented semi-automatically with the ITK-SNAP software. Using clinically recommended dose constraints and a standard simulated annealing algorithm, an optimized dose distribution could be calculated which met all prior constraints and was clinically realistic. The following chapter applies this model observer to optimize simulation CT image quality for an IMRT prostate treatment.

CHAPTER 6: MODEL OBSERVER APPLICATION & ANALYSIS

Having constructed a fully functional framework that resembles a model observer for radiation therapy, the aim of this chapter is to demonstrate the usage and limitations of this model observer. First, the model observer will be demonstrated by optimizing CT image quality for an IMRT prostate treatment. Treatment efficacy will be maintained while minimizing imaging dose, and an image reconstruction parameter will be optimized to yield maximum treatment efficacy. Secondly, the newly proposed model observer will be compared to other IQA metrics to display the improved performance when the appropriate task of radiation therapy is considered. Finally, the model observer will be analyzed for sources of bias and randomness. This is needed as several parameters (e.g. radiobiological modeling, image segmentation) were fixed for framework execution, and due to the fact that calculation randomness is introduced by the dose optimization algorithm.

A. Application 1: Optimization of imaging dose

One topic of interest within the radiation therapy community is the evaluation of imaging dose, particularly with the increase in image-guidance;[60, 61] this will be increasingly true as treatment survival rates improve. Moreover, for younger patients the risk of secondary induced cancer should also be strongly considered.[62, 63] Therefore the model observer was applied to optimize CT

imaging dose for radiation therapy, with the goal of minimizing imaging dose while still maintaining treatment plan efficacy. The AUTOC was calculated for a variety of imaging protocols of varying dose, achieved by altering the kVp of the imaging source and the number of initial photons from the source (variable I_0 in Eqn. 31). To compare different scan protocols, a relative $CTDI_{vol}$ was employed:

$$\frac{CTDI_{vol,i}}{CTDI_{vol,min}} = \left(\frac{N_i}{N_{min}}\right) \times \left(\frac{kVp_i}{kVp_{min}}\right)^2 \quad (48)$$

A relative metric is proposed since the CT acquisition process was not calibrated to directly calculate imaging dose. The number of photons I_0 was varied using values of 5 x 10^3, 7.5 x 10^3, 1.0 x 10^4, 2.5 x 10^4, 5.0 x 10^4, 7.5 x 10^4, 1.0 x 10^5, and 2.5 x 10^5 photons per detector element. Similarly, the kVp was varied using values of 80, 100, 120, and 140 kVp. The AUTOC was calculated for each of the acquired image sets and plotted as a function of relative $CTDI_{vol}$.

B. Application 2: Optimization of CT reconstruction algorithms

Another interesting challenge in the medical imaging is the optimization of CT reconstruction algorithms, including traditional FBP methods [insert reference] and more recently developed iterative reconstruction algorithms.[64, 65] Thus the model observer will also be applied to optimize CT FBP reconstruction for radiation therapy. Specifically, the filter parameter *a* in Eqn. 35 was varied, taking values of 2, 4, 6, 8, and 10, and the AUTOC will be calculated for each parameter value, for low-dose CT images. The ramp filter implementation (i.e. $a \approx 0$) was excluded as the low-dose images were too noisy for adequate

segmentation and treatment planning. This application will enable the analysis of the trade-off between image noise and spatial resolution (as described in Chapter 4) and its effect on the radiation therapy treatment. The AUTOC was calculated for each image set acquired using the aforementioned filter parameters, with a kVp of 140 and the number of photons per detector element set to 5×10^3. The AUTOC was then plotted as a function of *a*.

C. Analysis 1: Comparison to other IQA metrics

In order to evaluate the importance of the AUTOC as a FOM for radiation therapy IQA, a comparison was made to other IQA metrics as mentioned in Chapter 2. Specifically, the AUTOC will be compared to the CNR, SSIM, and NEQ. This will aid in determining the effectiveness of the AUTOC and proving whether or not additional image quality assessment information is obtained when the appropriate task is considered.

The CNR was calculated using Eqn. 3, with ROIs placed in the signal (prostate) and background of the generated patient images as shown in Figure 21 (left image). The mean SSIM was calculated using Eqn. 9 for each of the images in a patient data set; these values were then averaged together to produce a singular value per patient data set which was used for comparison; Figure 22 displays a sample SSIM calculation.

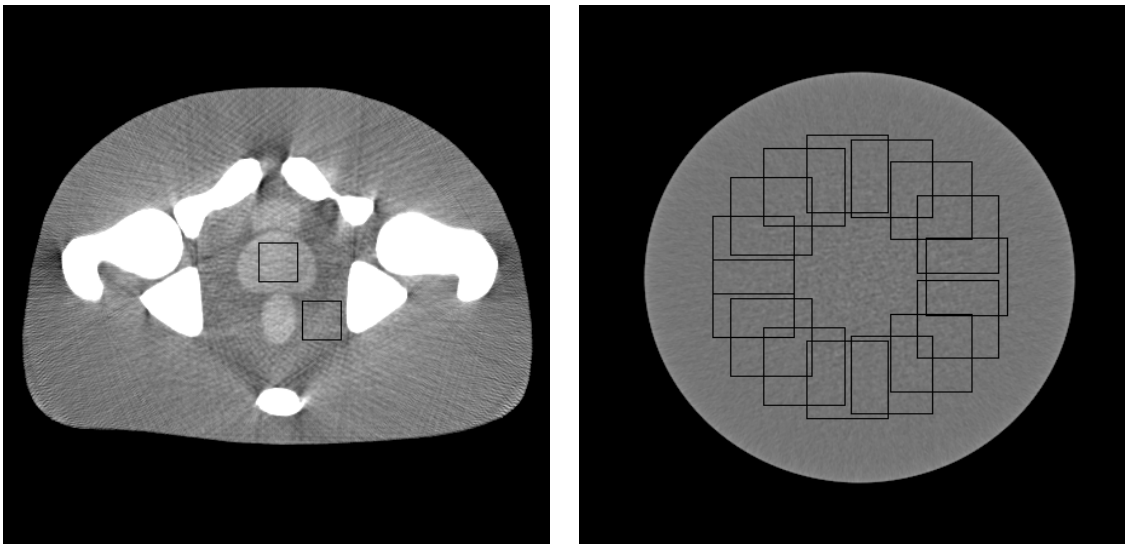

Figure 21. ROI placement for CNR (left) and NPS (right) calculation.

To calculate the NEQ, the MTF and NPS were first calculated separately, followed by application of Eqn. 20. To calculate the MTF and NPS, the approach of Friedman *et al*.,[66] in addition to our previously conducted work,[5] was implemented on the computer-generated CT data. For each of the scan acquisition parameter sets listed in Sections 6.A. and 6.B., helical CT images of a cylindrical water phantom were generated. For MTF calculation the ESF was obtained from the edge of the cylindrical phantom, followed by the methodology described in Section 2.C. NPS calculation was performed using Eqn. 6, with square ROIs having dimensions of 64 x 64 pixels placed equidistant from the phantom center, as shown in Figure 21. The radial bin size used to produce the 1D NPS was selected as 0.025 mm^{-1}. This choice was determined by manual tuning to obtain appropriate spectral smoothness. In practice, the magnitude of the NPS at the spatial frequency origin is difficult to estimate accurately for finite

data, as has been reported in previous literature.[67] Since the radial, 1D NPS varies linearly at low spatial frequencies, the zero-frequency value of the 1D NPS in this study was estimated via linear extrapolation.

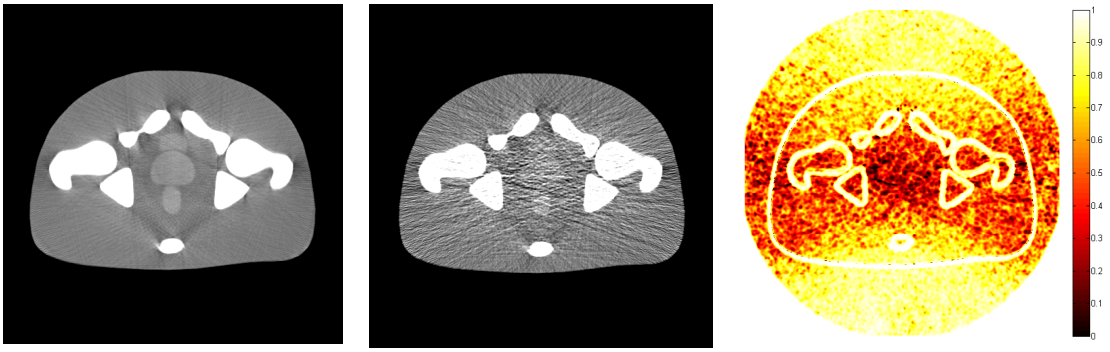

Figure 22. A sample SSIM map calculation for the acquired CT images. The gold standard image (left) is compared to the test image (right) to compute the SSIM map (right). The mean SSIM for this test data set was 0.7593.

As the segmentation accuracy plays an important role in treatment plan quality, the comparison of AUTOC with segmentation accuracy was also performed in addition to the IQA metrics. Each of the segmented organs was compared to the corresponding organ of the ground truth object model using Dice's similarity coefficient (DSC). The calculated values of DSC were plotted against AUTOC for each of the scans listed in Sections 6.A. and 6.B.

D. Analysis 2: Sources of randomness

The initial derivation of the TOC curve, as described in Section 2.D. and summarized by Eqn. 25, is predicated on a non-random dose calculation algorithm. However, as stated in Section 5.D., the simulated annealing algorithm

utilizes a random number generator to select the beamlet number and grain sign. In order to study the randomness introduced into the AUTOC calculation, the simulated annealing algorithm was performed several times for one image dataset, and the subsequent AUTOC was calculated until a sufficient sample size was obtained.

E. Analysis 3: Sources of bias

The AUTOC is directly dependent on the TCP and NTCP, which is often calculated using one of several radiobiological model. To study the bias in the AUTOC introduced by the radiobiological model, the AUTOC was calculated using two additional models, as referenced by Warkentin *et al*.,[68] and compared to the EUD-based calculation of the TCP and NTCP. First, a Poisson-based model for TCP calculation is utilized:

$$TCP = \left(\frac{1}{2}\right)^{x}, \quad x = \sum_{i} v_i \times exp[2\gamma_{50}(1 - D_i/D_{50})/ln2]. \tag{49}$$

Second, the NTCP was calculated using a sigmoidal dose response (SDR) model:

$$NTCP = \Phi\left(\frac{EUD - D_{50}}{mD_{50}}\right), \quad \Phi(x) = \frac{1}{2}\left[1 + erf\left(\frac{x}{\sqrt{2}}\right)\right]. \tag{50}$$

Combined with the EUD-based TCP and NTCP calculations, this yields four possible combinations of TCP-NTCP calculations: EUD-EUD, Poisson-EUD, EUD-SDR, and Poisson-SDR. The AUTOC was calculated for all four combinations and compared for varying dose and reconstruction filter, as in

Sections A and B. In addition to the choice of model type, it is also known that the TCP/NTCP calculation is sensitive to the choice of parameter values used within the model. Thus the EUD-based TOC was calculated while varying parameters γ_{50} and TCD_{50} for different prostate cancer stages. These calculated values for the AUTOC were also compared for varying dose and reconstruction filter.

F. Results & Discussion

Figure 23 displays the AUTOC as a function of the imaging dose, along with other relevant IQA metrics. It is apparent that at a certain imaging dose threshold the treatment plan efficacy becomes unacceptable, as the AUTOC approaches near zero values for low-dose images. However, as the imaging dose increases, the AUTOC rises to near unity, indicating an acceptable treatment plan efficacy. For very high imaging doses, the increased benefit in treatment plan quality is minimal. By comparison, the other IQA metrics gradually decrease as the dose decreases. Thus when using the AUTOC as a FOM for task-based IQA a minimum imaging dose which maintains treatment plan quality can be objectively determined, while this threshold is difficult to determine when using IQA metrics that are not appropriate for the task. When looking at the zoomed-in version on the right in Figure 23, it can be observed that the AUTOC reaches a maximum value for a relative dose of 10, and then unexpectedly decreases as the dose increases. We hypothesize that this is due to the increase

in beam hardening artifacts, which are obscured in part by image noise in the lower dose images; further investigation is warranted to assess this.

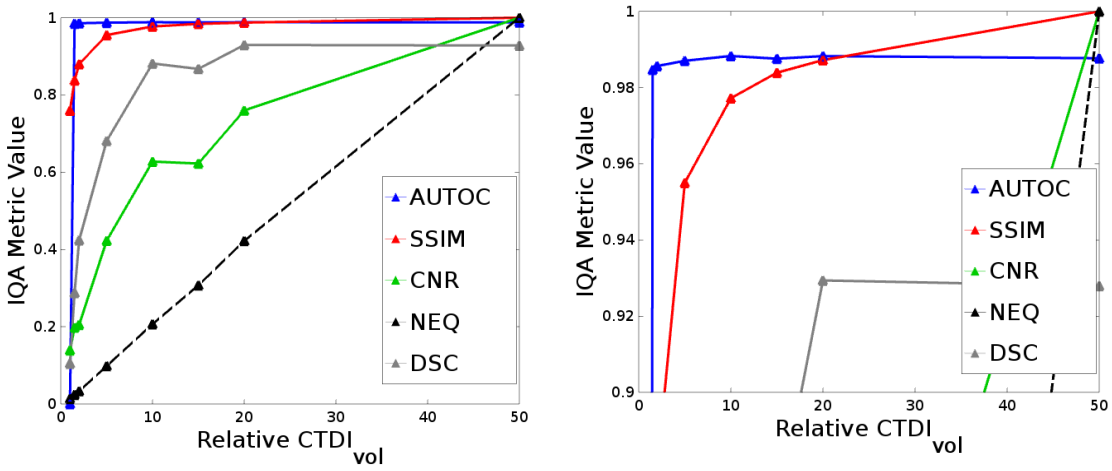

Figure 23. The AUTOC compared to various IQA metrics as a function of CT imaging dose, in terms of a relative $CTDI_{vol}$. The full image is provided (left) along with a zoomed-in version (right) to help distinguish the higher AUTOC values.

Figure 24 displays the AUTOC as a function of the filter parameter *a*, along with other relevant IQA metrics. As with the imaging dose, images reconstructed using a filter parameter value of 2 are not suitable for patient treatments. The AUTOC then increases as *a* increases, reaching a maximum for a filter parameter value of 6. Finally, due to the over-smoothing of the high *a* value images, the AUTOC decreases, albeit only slightly, as the filter parameter increases beyond *a* = 6. Thus the proposed model observer can be used to objectively select an optimal value for the FBP reconstruction filter, which is optimal in the sense that it maximizes patient treatment efficacy. When comparing the AUTOC to the other IQA metrics and the DSC, it can be seen that

different optimal values for *a* are obtained, which depend on the desired task. When image quality is being assessed based on image contrast and noise (CNR) or signal detectability (NEQ), the most optimal reconstruction occurs when *a* = 10, corresponding to the images with the least amount of noise. Likewise, when the task is segmentation accuracy (DSC), the most optimal reconstruction occurs when *a* = 8. Thus reconstruction filter optimization is task-dependent, and if images are to be optimized for radiation therapy the appropriate task (patient treatment efficacy) must be considered.

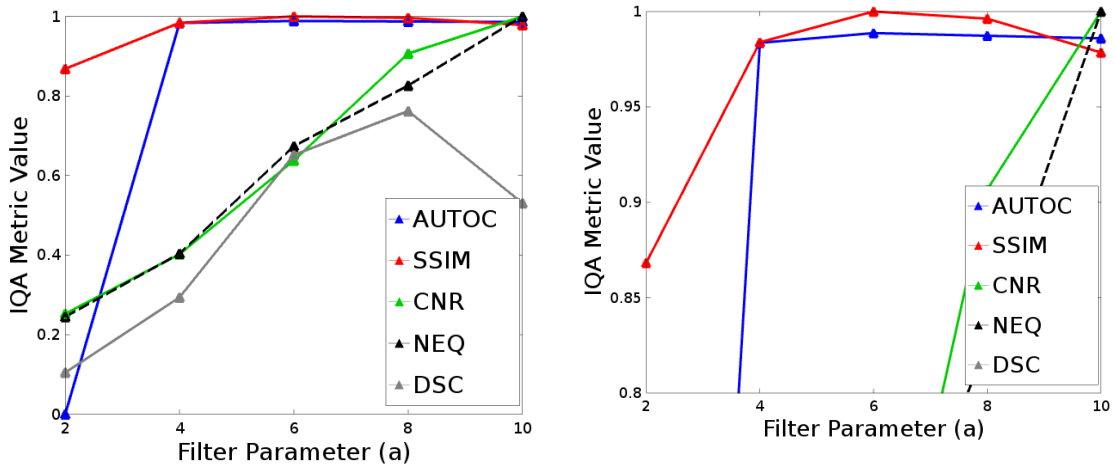

Figure 24. The AUTOC compared to various IQA metrics for different image reconstructions, in terms of the filter parameter *a*. The full image is provided (left) along with a zoomed-in version (right) to help distinguish the higher AUTOC values.

Figure 25 displays the effect of radiobiological model and model parameters on the AUTOC. While the AUTOC values differ when utilizing different models and model parameters, the rank order remains the same. For example, the optimal reconstruction filter occurs when *a* = 6 no matter which

model or model parameters are chosen. In addition, after a sufficient sample size was determined, AUTOC variation introduced by the dose optimization algorithm was approximately 0.02%, at the 95% confidence interval. Thus the proposed model observer is relatively insensitive to the randomness and bias analyzed in this study.

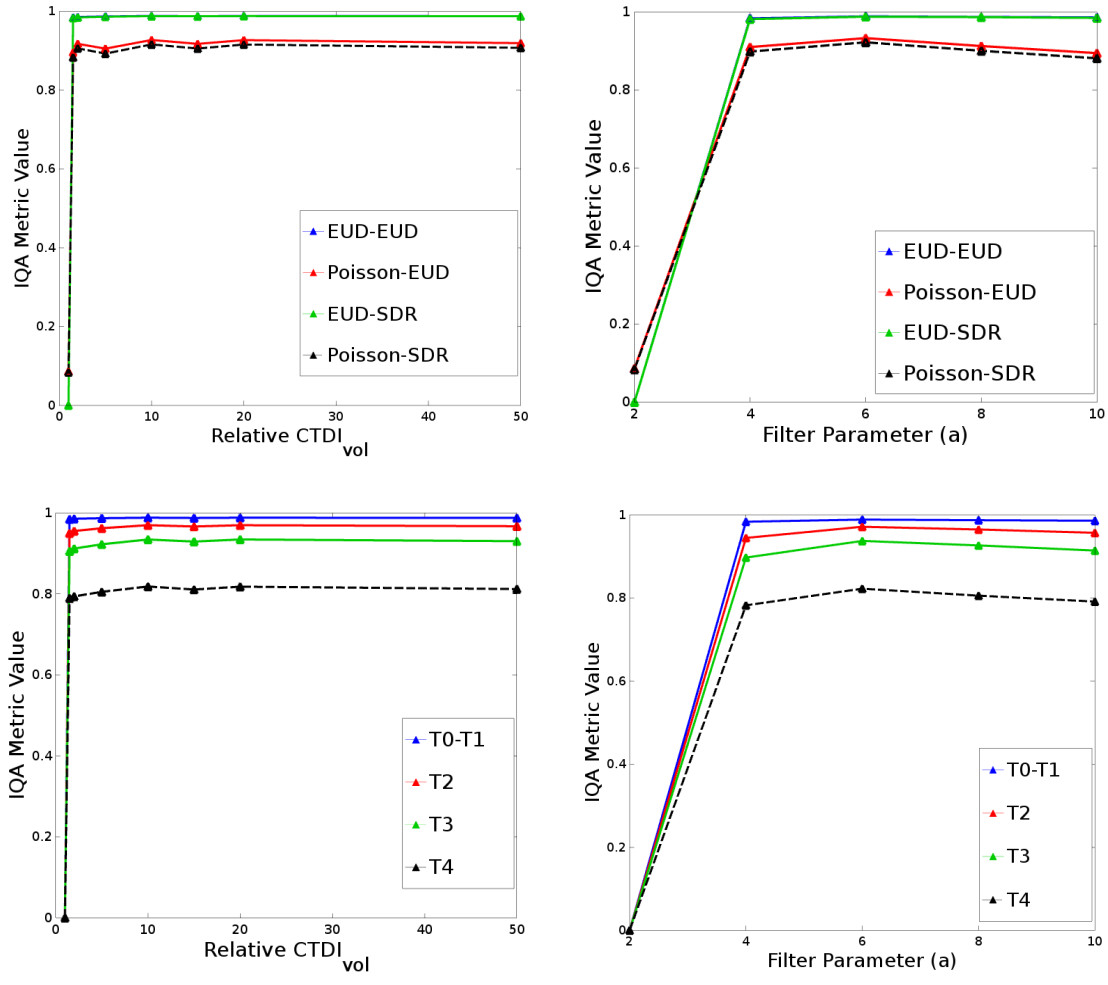

Figure 25. Analysis of the radiobiological model bias within the AUTOC calculation. The top row displays AUTOC calculation for different radiobiological models, while the bottom row displays the AUTOC calculated using different model parameters according to different prostate cancer stages.

This chapter provided a demonstration of the newly proposed model observer, followed by comparison to other IQA metrics and analysis of sources of randomness and bias. Both CT imaging dose and the FBP image reconstruction filter were optimized for the task of radiation therapy. The optimal value for image reconstruction when using the proposed model observer differed compared to other IQA metrics, indicating that optimization is task-dependent and that the appropriate task must be considered. The randomness introduced by the simulated annealing algorithm, in addition to the bias from radiobiological models and model parameters, did not have an effect on the calculated AUTOC.

CHAPTER 7: CONCLUSIONS AND FUTURE WORK

A model observer has been developed and implemented to assess image quality based on radiation therapy treatment efficacy. It enables objective determination of appropriate imaging parameter values, both for imaging dose and image reconstruction. Framework flexibility allows for incorporation of additional modules to include any aspect of the treatment process, and therefore has great potential for both assessment and optimization within radiation therapy. This chapter concludes this dissertation by providing a summary of contributions and a discussion of the future direction for this work.

A. Summary of Contributions

In Chapter 1, the general concepts relevant to image quality assessment for radiation therapy are introduced. The expansive role of medical imaging within radiation therapy necessitates a thorough assessment of image quality, but the currently available image quality assessment methodology does not consider the task of radiation therapy. Therefore this study proposes a new model observer capable of task-based image quality assessment in radiation therapy.

Chapter 2 builds upon this premise by providing a detailed description of the currently available IQA methods and metrics. The physically-based metrics such as the mean, standard deviation, and contrast-to-noise ratio are readily obtainable but not task-based. The human visual system (HVS) based models

are also readily obtainable and in addition can objectively quantify human image perception, but cannot compare images that are structurally dissimilar and are still not task-based metrics. While the task-based IQA methodology for diagnostic imaging improves upon these previous two categories by linking image quality to clinical task performance, the task of disease diagnosis (i.e. binary classification) is not suitable for radiation therapy. Theory for the evaluation of radiation therapy treatments using the area under the TOC curve is presented, which provides a suitable figure of merit for the newly proposed model observer.

Chapter 3 introduces this model observer, with general guidelines given for strategy and implementation. Given computer generated images of a numerical phantom, the model observer designs and delivers an optimal radiation therapy treatment plan, and then evaluates that plan using the AUTOC, calculated from the optimized dose distribution and the organ boundaries of the numerical phantom. From a software standpoint, the model observer was constructed using the object-oriented programming paradigm, creating encapsulated modules for each step of the radiation therapy treatment planning process. As an initial demonstration, prostate cancer patient was chosen as the treatment site, with IMRT as the chosen treatment modality.

Chapter 4 begins the detailed explanation of the model observer implementation by describing the generation of both the object model and the CT images. Since the current methodologies for numerical phantom generation do not allow the creation of a statistical ensemble of realistic patient phantoms, a

new methodology was created and applied which utilized geometric attribute distribution (GAD) models. Helical projection data was generated from these object models using exponential attenuation, and the projection data was reconstructed using a traditional filtered backprojection algorithm for fan-beam data. Both the imaging exposure (i.e. number of photons) and the Fourier-domain reconstruction filter were adjustable, enabling an optimization of these parameters for radiation therapy. The object model and images were deemed realistic both subjectively and objectively.

Having created a means to generate realistic images of a known object model, Chapter 5 proceeds to implement the model observer for radiation therapy. A simulation framework was constructed which emulates an end-to-end external beam radiation therapy treatment. Given the generated CT images, image segmentation was performed semi-automatically using geodesic active contours via the ITK-SNAP software. During the treatment planning phase, the number of beams and treatment isocenter were selected automatically, and the planned dose was calculated using a Monte Carlo dose calculation engine (DPM) and optimized using a simulated annealing technique. Following the emulation of the end-to-end treatment, the model observer then estimates the treatment outcome via radiobiological modeling, producing the AUTOC. The optimized dose distributions matched all realistic clinical constraints.

Finally, in Chapter 6 the newly constructed model observer is applied by optimizing imaging dose and image reconstruction for the task of radiation

therapy. The superiority of the model observer was also demonstrated by comparison to the other IQA metrics (physically-based, HVS-based, and diagnostic task-based). To gain a fuller understanding of the model observer, sources of bias and randomness were also assessed. Specifically, the bias introduced by the choice of radiobiological model for TCP/NTCP calculation was assessed, in addition to the randomness in the AUTOC caused by the randomized simulated annealing algorithm. Both the randomness and bias analyzed in this study had little effect on the calculated AUTOC.

B. Future Directions

While this dissertation project is comprehensive in the sense that an end-to-end radiation therapy treatment is simulated, from object to treatment outcome analysis, there proposed model observer does not include all aspects of a radiation therapy treatment. This section will therefore state future directions both for new improvements and new applications for the currently proposed model observer.

In this study, a method for generating CT images of the numerical phantoms was provided here as a demonstration, but other imaging modalities can be included if the appropriate intrinsic physical properties are considered. For example, each organ could be assigned a proton density value in addition to attenuation coefficients, and the transport of radiofrequency waves through tissue could be simulated to produce MRI acquisitions. Similar simulations could also

be performed for CBCT and ultrasound imaging. Using multimodality imaging of the proposed numerical phantoms, and subsequent incorporation into the model observer simulation, any imaging modality could be assessed within this framework for the task of radiation therapy. Specifically, assessment of image quality can be performed both for currently challenging imaging modalities such as CBCT (due to photon scatter),[69, 70] in addition to newly developed technologies such as MRI-guided radiation therapy.[71]

This study applied the GAD models to quantify the inter-patient statistical variations, both in organ shape and position. However, the GAD models can also be extended to incorporate intra-patient variations, including inter- and intra-fraction patient motion, if adequate image data (e.g. daily CBCT, MRI) can be obtained. Training GAD models to quantify inter-and intra-fraction patient motion will allow for the inclusion of patient motion and image guidance modules within the model observer framework, and will be an ongoing work of this project.

When considering the creation of numerical phantoms proposed in this study, one limitation of the current methodology is the absence of muscle tissue, as it is typically not segmented for treatment due to its radio-resistant nature. While muscle tissue does not affect the treatment directly in that muscle is not segmented or included in the treatment plan dose constraints, the increased attenuation of muscle when compared to adipose tissue may affect the image contrast and/or noise of the relevant tissues. Future work includes the simulation

of muscle tissue by another means, in addition to increasing model robustness by supplying additional training datasets from the retrospective patient cases.

Within the model observer implementation schematics of Figure 7, improvements of the individual modules can also be performed. First, it is desirable to integrate automatic segmentation into the framework without use of third party applications, to increase simulation automation. This could be accomplished using the aforementioned ITK library.[40] Second, while the static IMRT treatment implemented in this study is a common treatment technique, many other modalities exist such as brachytherapy and other external beam treatments, and these modalities should be included so that IQA can be performed for each specific modality. Finally, while the AUTOC is presented here as the FOM, there is some question as to the viability of the *in vitro* radiobiological models when compared to the *in vivo* patient results; other treatment outcome metrics[72, 73] will be assessed as viable FOMs.

In regards to framework computational performance, there are some calculation aspects that are prohibitively expensive in terms of computational time. Specifically, the computation of CT projection data acquisition and DPM dose calculation require ~10 and ~4 hours, respectively. However, in this study only minimal CPU optimization (with OpenMP) was implemented; further code optimization can be conducted, in addition to the use of GPU programming,[74, 75] to decrease calculation time and increase model observer tractability.

In conclusion, a model observer was created and applied to assess images based on the task of radiation therapy. Beginning with the known organ boundaries of a simulated patient, an end-to-end radiation therapy treatment was simulated, automatically designing and delivering an optimized radiation dose to the patient using the available CT images. This plan was evaluated using patient treatment outcome modeling with the known organ boundaries. Thus CT image quality was linked directly to patient treatment efficacy. Application of the newly proposed model observer demonstrated that CT image quality optimization is task-dependent, and the specific task of radiation therapy should be considered as a part of the optimization process. Future work will consist of improving current modules within the model observer framework and the inclusion of additional modules to assess the variety of imaging modalities within radiation therapy.

REFERENCES

1 M. Hodaie and A.F. Coello, “Advances in the management of trigeminal neuralgia,” J. Neurosurg. Sci. **57**(1), 13–21 (2013).

2 Z.A. Smith *et al.*, “Dedicated linear accelerator radiosurgery for trigeminal neuralgia: a single-center experience in 179 patients with varied dose prescriptions and treatment plans,” Int. J. Radiat. Oncol. Biol. Phys. **81**(1), 225–231 (2011).

3 F.M. Khan and J.P. Gibbons, *Khan’s The Physics of Radiation Therapy* (Lippincott Williams & Wilkins, 2014).

4 J. Xu, D.D. Reh, J.P. Carey, M. Mahesh, and J.H. Siewerdsen, “Technical assessment of a cone-beam CT scanner for otolaryngology imaging: image quality, dose, and technique protocols,” Med. Phys. **39**(8), 4932–4942 (2012).

5 S. Dolly, H. Chen, M. Anastasio, S. Mutic, and H. Li, “TU-EF-204-10: A Preliminary Study Evaluating Calculation Variations of Local Noise Power Spectra for CT Simulation in Radiation Therapy,” Med. Phys. **42**(6), 3622–3622 (2015).

6 Z. Wang, A.C. Bovik, H.R. Sheikh, and E.P. Simoncelli, “Image quality assessment: from error visibility to structural similarity,” IEEE Trans. Image Process. **13**(4), 600–612 (2004).

7 J. Miao, D. Huo, and D.L. Wilson, “Quantitative image quality evaluation of MR images using perceptual difference models,” Med. Phys. **35**(6), 2541–2553 (2008).

8 H.H. Barrett and K.J. Myers, *Foundations of Image Science* (John Wiley & Sons, 2013).

9 W. Vennart, “ICRU Report 54: Medical imaging—the assessment of image quality,” Radiography **3**(3), 243–244 (1997).

10 H.H. Barrett, M.A. Kupinski, S. Müeller, H.J. Halpern, J.C. Morris 3rd, and R. Dwyer, “Objective assessment of image quality VI: imaging in radiation therapy,” Phys. Med. Biol. **58**(22), 8197–8213 (2013).

11 H.H. Barrett *et al.*, “Therapy Operating Characteristic (TOC) Curves and their Application to the Evaluation of Segmentation Algorithms,” Proc. SPIE Int. Soc. Opt. Eng. **7627**, 76270Z (2010).

12 J.T. Bushberg, *The Essential Physics of Medical Imaging* (Lippincott Williams & Wilkins, 2002).

13 M.M. Goodsitt, H.-P. Chan, T.W. Way, S.C. Larson, E.G. Christodoulou, and J. Kim, “Accuracy of the CT numbers of simulated lung nodules imaged with multi-detector CT scanners,” Med. Phys. **33**(8), 3006–3017 (2006).

14 J.H. Siewerdsen, I.A. Cunningham, and D.A. Jaffray, “A framework for noise-power spectrum analysis of multidimensional images,” Med. Phys. **29**(11), 2655–2671 (2002).

15 A.R. Pineda, D.J. Tward, A. Gonzalez, and J.H. Siewerdsen, “Beyond noise power in 3D computed tomography: the local NPS and off-diagonal elements

of the Fourier domain covariance matrix," Med. Phys. **39**(6), 3240–3252 (2012).
16 *http://www.cns.nyu.edu/lcv/ssim/*, (n.d.).
17 *IAB*, (n.d.).
18 *DCTune 2.0 README*, (n.d.).
19 R.F. Wagner and D.G. Brown, "Unified SNR analysis of medical imaging systems," Phys. Med. Biol. **30**(6), 489–518 (1985).
20 W.P. Segars, M. Mahesh, T.J. Beck, E.C. Frey, and B.M.W. Tsui, "Realistic CT simulation using the 4D XCAT phantom," Med. Phys. **35**(8), 3800 (2008).
21 X.G. Zu and X. George Zu, "The VIP-Man Model – A Digital Human Testbed for Radiation Siimulations," in *SAE Technical Paper Series*(2005).
22 *Thorax Phantom*, (n.d.).
23 J. Zhu, Z. Jiehua, Z. Shiying, Y. Yangbo, and W. Ge, "Computed tomography simulation with superquadrics," Med. Phys. **32**(10), 3136 (2005).
24 H.-C. Chen *et al.*, "Automated contouring error detection based on supervised geometric attribute distribution models for radiation therapy: a general strategy," Med. Phys. **42**(2), 1048–1059 (2015).
25 A. Tsai, W. Wells, C. Tempany, E. Grimson, and A. Willsky, "Mutual information in coupled multi-shape model for medical image segmentation," Med. Image Anal. **8**(4), 429–445 (2004).
26 J. Yang, L.H. Staib, and J.S. Duncan, "Neighbor-constrained segmentation with level set based 3-D deformable models," IEEE Trans. Med. Imaging **23**(8), 940–948 (2004).
27 *FileZilla - The free FTP solution*, (n.d.).
28 *LibArchive for Windows*, (n.d.).
29 I.L. Dryden, M.R. Faghihi, and C.C. Taylor, "Procrustes Shape Analysis of Planar Point Subsets," J. R. Stat. Soc. Series B Stat. Methodol. **59**(2), 353–374 (1997).
30 P. Cignoni, *MeshLab*, (n.d.).
31 H. Hoppe and H. Hugues, "Poisson surface reconstruction and its applications," in *Proceedings of the 2008 ACM symposium on Solid and physical modeling - SPM '08*(2008).
32 M. Garland, G. Michael, and P.S. Heckbert, "Surface simplification using quadric error metrics," in *Proceedings of the 24th annual conference on Computer graphics and interactive techniques - SIGGRAPH '97*(1997).
33 G. Taubin and T. Gabriel, "A signal processing approach to fair surface design," in *Proceedings of the 22nd annual conference on Computer graphics and interactive techniques - SIGGRAPH '95*(1995).
34 J.M. Boone and J.A. Seibert, "An accurate method for computer-generating tungsten anode x-ray spectra from 30 to 140 kV," Med. Phys. **24**(11), 1661–1670 (1997).
35 N. US Department of Commerce, *NIST: X-Ray Mass Attenuation Coefficients*, (2009).
36 T. Möller, M. Tomas, and T. Ben, "Fast, minimum storage ray/triangle intersection," in *ACM SIGGRAPH 2005 Courses on - SIGGRAPH '05*(2005).

37 K. Taguchi, T. Katsuyuki, and A. Hiroshi, “Algorithm for image reconstruction in multi-slice helical CT,” Med. Phys. **25**(4), 550 (1998).
38 A.C. Kak and M. Slaney, *Principles of Computerized Tomographic Imaging* (SIAM, 2001).
39 M. Frigo and S.G. Johnson, “The Design and Implementation of FFTW3,” Proc. IEEE **93**(2), 216–231 (2005).
40 T.S. Yoo *et al.*, “Engineering and algorithm design for an image processing Api: a technical report on ITK--the Insight Toolkit,” Stud. Health Technol. Inform. **85**, 586–592 (2002).
41 P.A. Yushkevich *et al.*, “User-guided 3D active contour segmentation of anatomical structures: significantly improved efficiency and reliability,” Neuroimage **31**(3), 1116–1128 (2006).
42 V. Caselles, R. Kimmel, and G. Sapiro, “Geodesic active contours,” in *Proceedings of IEEE International Conference on Computer Vision*(n.d.).
43 F.M. Khan and B.J. Gerbi, *Treatment Planning in Radiation Oncology* (Lippincott Williams & Wilkins, 2011).
44 J. Sempau, S.J. Wilderman, and A.F. Bielajew, “DPM, a fast, accurate Monte Carlo code optimized for photon and electron radiotherapy treatment planning dose calculations,” Phys. Med. Biol. **45**(8), 2263–2291 (2000).
45 B. Vanderstraeten *et al.*, “Conversion of CT numbers into tissue parameters for Monte Carlo dose calculations: a multi-centre study,” Phys. Med. Biol. **52**(3), 539–562 (2007).
46 S. Webb, “Optimization by simulated annealing of three-dimensional conformal treatment planning for radiation fields defined by a multileaf collimator,” Phys. Med. Biol. **36**(9), 1201–1226 (1991).
47 D.M. Shepard, M.A. Earl, X.A. Li, S. Naqvi, and C. Yu, “Direct aperture optimization: a turnkey solution for step-and-shoot IMRT,” Med. Phys. **29**(6), 1007–1018 (2002).
48 D. Shreiner and O.A.R. Board, *OpenGL Programming Guide: The Official Guide to Learning OpenGL, Version 2.1* (Addison-Wesley Professional, 2008).
49 K.D. Held, “Radiobiology for the Radiologist, 6th ed., by Eric J. Hall and Amato J. Giaccia,” Radiat. Res. **166**(5), 816–817 (2006).
50 A. Niemierko and N. Andrzej, “Reporting and analyzing dose distributions: A concept of equivalent uniform dose,” Med. Phys. **24**(1), 103 (1997).
51 H.A. Gay and A. Niemierko, “A free program for calculating EUD-based NTCP and TCP in external beam radiotherapy,” Phys. Med. **23**(3-4), 115–125 (2007).
52 S. Rana and C. Cheng, “Radiobiological impact of planning techniques for prostate cancer in terms of tumor control probability and normal tissue complication probability,” Ann. Med. Health Sci. Res. **4**(2), 167–172 (2014).
53 G.O. De Meerleer, L.A.M.L. Vakaet, W.R.T. De Gersem, C. De Wagter, B. De Naeyer, and W. De Neve, “Radiotherapy of prostate cancer with or without intensity modulated beams: a planning comparison,” International Journal of Radiation Oncology*Biology*Physics **47**(3), 639–648 (2000).

54 L. Boersma *et al.*, “Estimation of the Incidence of Late Bladder and Rectum Complications After High-Dose (70–78 Gy) Conformal Radiotherapy for Prostate Cancer, Using Dose–Volume Histograms,” International Journal of Radiation OncologyBiologyPhysics **41**(1), 83–92 (1998).
55 M.G. Witte, J. van der Geer, C. Schneider, J.V. Lebesque, M. Alber, and M. van Herk, “IMRT optimization including random and systematic geometric errors based on the expectation of TCP and NTCP,” Med. Phys. **34**(9), 3544–3555 (2007).
56 G. Sharp *et al.*, “Vision 20/20: perspectives on automated image segmentation for radiotherapy,” Med. Phys. **41**(5), 050902 (2014).
57 C.G. Orton, T.R. Bortfeld, A. Niemierko, and J. Unkelbach, “The role of medical physicists and the AAPM in the development of treatment planning and optimization,” Med. Phys. **35**(11), 4911–4923 (2008).
58 O. Acosta *et al.*, “Evaluation of multi-atlas-based segmentation of CT scans in prostate cancer radiotherapy,” in *2011 IEEE International Symposium on Biomedical Imaging: From Nano to Macro*(2011).
59 A. Isambert *et al.*, “Evaluation of an atlas-based automatic segmentation software for the delineation of brain organs at risk in a radiation therapy clinical context,” Radiother. Oncol. **87**(1), 93–99 (2008).
60 M.J. Murphy *et al.*, “The management of imaging dose during image-guided radiotherapy: report of the AAPM Task Group 75,” Med. Phys. **34**(10), 4041–4063 (2007).
61 D.W. Kim, W.K. Chung, and M. Yoon, “Imaging doses and secondary cancer risk from kilovoltage cone-beam CT in radiation therapy,” Health Phys. **104**(5), 499–503 (2013).
62 Y. Zhang *et al.*, “Concomitant Imaging Dose and Cancer Risk in Image Guided Thoracic Radiation Therapy,” Int. J. Radiat. Oncol. Biol. Phys. **93**(3), 523–531 (2015).
63 A.S. Brody, D.P. Frush, W. Huda, R.L. Brent, and And The Section, “Radiation Risk to Children From Computed Tomography,” Pediatrics **120**(3), 677–682 (2007).
64 J.-B. Thibault, K.D. Sauer, C.A. Bouman, and J. Hsieh, “A three-dimensional statistical approach to improved image quality for multislice helical CT,” Med. Phys. **34**(11), 4526–4544 (2007).
65 L. Ritschl, F. Bergner, C. Fleischmann, and M. Kachelriess, “Improved total variation-based CT image reconstruction applied to clinical data,” Phys. Med. Biol. **56**(6), 1545–1561 (2011).
66 S.N. Friedman, G.S.K. Fung, J.H. Siewerdsen, and B.M.W. Tsui, “A simple approach to measure computed tomography (CT) modulation transfer function (MTF) and noise-power spectrum (NPS) using the American College of Radiology (ACR) accreditation phantom,” Med. Phys. **40**(5), 051907 (2013).
67 B. Chen, O. Christianson, J.M. Wilson, and E. Samei, “Assessment of volumetric noise and resolution performance for linear and nonlinear CT reconstruction methods,” Med. Phys. **41**(7), 071909 (2014).

68 B. Warkentin, P. Stavrev, N. Stavreva, C. Field, and B.G. Fallone, “A TCP-NTCP estimation module using DVHs and known radiobiological models and parameter sets,” J. Appl. Clin. Med. Phys. **5**(1), 50–63 (2004).
69 J.-Y. Jin *et al.*, “Combining scatter reduction and correction to improve image quality in cone-beam computed tomography (CBCT),” Med. Phys. **37**(11), 5634–5644 (2010).
70 L. Ren, F.-F. Yin, I.J. Chetty, D.A. Jaffray, and J.-Y. Jin, “Feasibility study of a synchronized-moving-grid (SMOG) system to improve image quality in cone-beam computed tomography (CBCT),” Med. Phys. **39**(8), 5099–5110 (2012).
71 Y. Hu *et al.*, “Characterization of the onboard imaging unit for the first clinical magnetic resonance image guided radiation therapy system,” Med. Phys. **42**(10), 5828–5837 (2015).
72 K.S.C. Chao, A.I. Blanco, and J.F. Dempsey, “A conceptual model integrating spatial information to assess target volume coverage for IMRT treatment planning,” Int. J. Radiat. Oncol. Biol. Phys. **56**(5), 1438–1449 (2003).
73 L. Strigari, M. D’Andrea, A. Abate, and M. Benassi, “A heterogeneous dose distribution in simultaneous integrated boost: the role of the clonogenic cell density on the tumor control probability,” Phys. Med. Biol. **53**(19), 5257–5273 (2008).
74 X. Jia, X. Gu, Y.J. Graves, M. Folkerts, and S.B. Jiang, “GPU-based fast Monte Carlo simulation for radiotherapy dose calculation,” Phys. Med. Biol. **56**(22), 7017–7031 (2011).
75 A. Badal, B. Andreu, and B. Aldo, “Accelerating Monte Carlo simulations of photon transport in a voxelized geometry using a massively parallel graphics processing unit,” Med. Phys. **36**(11), 4878 (2009).

VITA

Steven Ray Dolly was born in Tallahassee, FL, on April 25, 1988, the son of Forrest Ray Dolly and Sharon Claire Dolly. After graduating from Leon High School, Steven attended Florida State University to study physics and received his bachelor of science in 2010. He then began studying within the field of medical physics at East Carolina University and completed his master of science degree in 2012. That same year Steven enrolled at the University of Missouri to study nuclear engineering, with a specific concentration in medical physics. Steven has been involved with research at Washington University in Saint Louis, and upon completion of his PhD will begin a therapeutic medical physics residency program at the University of Minnesota.